

Asynchronous Time-of-Arrival-Based 5G Localization: Methods and Optimal Geometry Analysis

Yuan Zhang^{ID}, Rui Wang^{ID}, Senior Member, IEEE, Erwu Liu, Senior Member, IEEE, Bofeng Li^{ID}, and Haibo Ge^{ID}

Abstract—This article is dedicated to addressing the localization challenge in 5G environments, specifically utilizing time-of-arrival (TOA) measurements. The focus is on scenarios where the user equipment (UE) and base transceiver stations (BTSs) or first-generation NodeBs (gNBs) face challenges related to synchronization or inaccurate BTS or gNB positions. First, we present the range-weighted majorization minimization (RW-MM) algorithm, harnessing majorization minimization (MM) techniques for UE localization. We rigorously establish the algorithm's monotonicity and demonstrate its convergence to a stationary point, providing a theoretical foundation for the RW-MM method. In addition, we present a novel UE localization method called robust range-weighted semidefinite relaxation (RRW-SDR). This method is specifically designed for situations involving bounded gNB position errors. The RRW-SDR algorithm optimizes the worst-case weighted least square function while uniquely addressing the individual error constraints associated with each gNB. Furthermore, we derive the Cramér–Rao lower bound (CRLB) for TOA-based UE localization. We additionally establish a more stringent lower bound on the determinant of the target estimation error covariance. This is particularly significant when dealing with scenarios that include independent measurement noise with varying variances. Moreover, we identify an optimal user-gNB geometrical configuration capable of achieving this lower bound. To validate the effectiveness and practical applicability of our contributions, we conduct a series of meticulous numerical simulations. These experiments affirm the robustness and utility of the developed methods.

Index Terms—5G localization, Cramér–Rao lower bound (CRLB), majorization minimization (MM), optimal sensor placement, semidefinite relaxation (SDR).

I. INTRODUCTION

THE FIFTH generation (5G) [1], [2] [also known as new radio (NR)] positioning, a breakthrough in cellular

Manuscript received 20 May 2024; revised 28 June 2024; accepted 24 July 2024. Date of publication 6 August 2024; date of current version 9 October 2024. This work was supported in part by the National Natural Science Foundation of China under Grant 62271352; in part by the Shanghai Science and Technology Innovation Action Plan Project under Grant 21220713100; and in part by the Natural Science Foundation of Shanghai under Grant 22ZR1465100. (*Corresponding author: Rui Wang*)

Yuan Zhang and Erwu Liu are with the College of Electronics and Information Engineering, Tongji University, Shanghai 201804, China (e-mail: yuanzhang@tongji.edu.cn; erwliu@tongji.edu.cn).

Rui Wang is with the College of Electronics and Information Engineering, and the Shanghai Institute of Intelligent Science and Technology, Tongji University, Shanghai 201804, China (e-mail: ruiwang@tongji.edu.cn).

Bofeng Li and Haibo Ge are with the College of Surveying and Geo-Informatics, Tongji University, Shanghai 200092, China (e-mail: bofeng_li@tongji.edu.cn; haibo_ge@tongji.edu.cn).

Digital Object Identifier 10.1109/JIOT.2024.3435958

navigation, revolutionizes location services. By leveraging advanced technologies like inertial navigation system (INS) and multiple next-generation NodeBs (gNBs) fusion, user equipment (UE) offers superior accuracy and reliability in determining a user's precise location. This innovation goes beyond traditional global navigation satellite systems (GNSSs), ensuring seamless navigation even in dense urban environments and indoors where GNSS signals may be weak. The integration of high-frequency bands and low-latency communication in UE enhances real-time tracking, making it a game changer for applications ranging from augmented reality to autonomous vehicles. In essence, UE positioning not only marks a significant milestone in wireless communication but also opens the door to a new era of precise and versatile location-based services.

In a network-based approach, the UE utilizes time-of-arrival (TOA) measurements from nearby base stations (BSs) to estimate its position, with the data being transmitted to a location server. Accurate UE localization can advance autonomous vehicles in 5G environments, thus elevating standards of safety and efficiency. Furthermore, it enables innovative solutions in augmented reality, industrial automation, and smart city initiatives. Nevertheless, this method presents certain drawbacks: first, it compromises user privacy as the UE location is disclosed even in nonemergency situations; second, localization services are confined to subscribers of a single cellular provider, limiting accessibility; and third, ambient cellular signals from other providers remain underutilized. To confront the challenges associated with 5G navigation, diverse methodologies have been explored. These encompass approaches, such as the joint estimation of biases with UE state, relying on UE motion or sensor fusion [3], [4], [5], and capitalizing on the relative frequency stability between base transceiver stations (BTSs) [6], [7]. Achieving synchronization becomes paramount when employing more BTSs for wireless positioning. Looking forward, the prospect of seamless navigation with 5G signals stands out as a promising technology to surmount these limitations without necessitating infrastructure changes [2]. This innovative approach holds the potential for enhancing privacy, expanding access to localization services, and maximizing the utilization of ambient cellular signals from various providers. Furthermore, ongoing research and collaborative efforts are likely to contribute to the refinement and widespread adoption of this promising navigational technology.

In contrast to GNSS, the states of a cellular 5G BTS remain unknown to a navigating UE and must be estimated. Despite the 3GPP standard indicating that a BTS should transmit its position, local wireless providers typically do not broadcast such information [8], [9]. Consequently, the positions of BTSSs need to be determined either through manual surveying or on-the-fly estimation, either individually or collaboratively [9], [10], [11]. A significant portion of the literature focusing on navigation using cellular signals involves the consideration of TOA and time difference of arrival (TDOA) measurements. However, certain assumptions, such as perfect synchronization or negligible variations between transmitter and UE clocks, are often made to simplify the measurement model, assuming the accurate knowledge of the BTS position [5], [12], [13], [14], [15], [16]. In practical scenarios, these assumptions may not hold true. Clock biases between the UE and BTS, as well as errors in the BTS position, must be taken into account to ensure accurate positioning. The challenge lies in addressing these practical considerations. In real-world situations, variations in clock synchronization and potential errors in BTS positions necessitate robust methods for estimating and compensating for these uncertainties.

Researchers have explored techniques to account for clock biases and enhance the overall accuracy of navigation using cellular signals. This ongoing research is essential for developing reliable and practical solutions that can effectively handle the complexities inherent in estimating the states of BTSSs and improve the accuracy of positioning systems utilizing cellular signals. In [17], the initialization of the UE's position and velocity state vectors, along with their corresponding covariances, relied on the output from the GNSS-INS system. Consequently, the system is not entirely stand-alone and exhibits limitations in terms of its application scenarios. The research presented in [18] employed a cellular network model utilizing a homogeneous Poisson point process (PPP) to establish bounds for TOA-based positioning. This model offers valuable insights into the performance expectations of localization within the context of both 4G and sub 6 GHz 5G networks. Simultaneously, an additional investigation detailed in [19] delved into the impact of signal-to-noise ratio (SNR) heterogeneity on TOA-based localization. This analysis utilized a binomial point process (BPP) model, contributing to a more comprehensive understanding of the localization performance under varying SNR conditions. It is important to note that these analyzes, while informative, operate under the assumption of synchronization between UE and BTSSs, a condition that may be impractical in real-world scenarios. Synchronization stands out as a critical factor influencing the accuracy of positioning techniques. Real-world networks often encounter challenges, such as asynchronous communication, which can significantly impact the performance of localization methods. Therefore, while the insights gained from these studies are valuable, further research is necessary to address the practical complexities of asynchronous systems, thereby enhancing the applicability of the findings to real-world cellular networks.

In the majority of research studies, it is generally assumed that the precise location of 5G BSs is known. For instance, the

work presented in [20] introduced cascaded extended Kalman filters (EKFs) that considered inevitable relative clock offsets. Exploring indoor positioning within the 5G NR framework, standardized and commercially operational in extensive markets, was addressed in [21]. This study proposed a solution and developed a software-defined radio UE for indoor positioning. The software-defined radio indoor positioning system sampled 5G NR signals using a universal software radio peripheral (USRP), and coarse synchronization was achieved by detecting the start of the synchronization signal block (SSB). In another study [22], a fusion method was devised to combine the estimated positions of a mobile station (MS) based on TDOA with the estimated position changes derived from temporal changes in carrier phase measurements. In more practical scenarios, there is a necessity to estimate the position of gNB, typically achieved by incorporating an additional GNSS module. Consequently, due consideration should have been given to the potential error in the gNB position.

Building upon the latest advancements in the field, this article presents the following contributions, summarized as follows.

- 1) We present a novel algorithm, range-weighted majorization minimization (RW-MM), specifically crafted for range-weighted least squares (R-WLSS) UE localization utilizing range measurements via the majorization minimization (MM) approach. This method takes into account the clock bias of both the UE and gNB. We have established the monotonicity of the algorithm and demonstrated its convergence to a stationary point, providing a rigorous foundation for the RW-MM approach.
- 2) We derive a novel UE localization method known as robust range-weighted semidefinite relaxation (RRW-SDR) that is designed to operate effectively in scenarios where bounded gNB position errors are present. This method maximizes the *worst-case* weighted LS function. Our approach stands out due to its individual treatment of the gNB position error constraint for each gNB, avoiding the need for further vectorized relaxation. This approach, which addresses each gNB's constraint separately, significantly enhances the accuracy of UE localization.
- 3) The Cramér–Rao lower bound (CRLB) for TOA-based UE localization measurements is derived. A tighter lower bound on the determinant of the target estimation error covariance is obtained for the independent measurement noise with nonidentical variances. An optimal UE-gNB geometrical placement that achieves the lower bound is derived.

Notations: Vectors, matrices, and their notations are vital in this context. They are denoted by bold lowercase letters (e.g., \mathbf{x}) and bold uppercase letters (e.g., \mathbf{X}). For a vector \mathbf{x} , its Euclidean norm is expressed as $\|\mathbf{x}\|$. In addition, the notations $\text{Tr}(\mathbf{X})$, $\det(\mathbf{X})$, and $\|\mathbf{X}\|$ represent the trace, determinant, and norm of a matrix, respectively. A diagonal matrix takes the form of $\text{diag}(\mathbf{x})$, where \mathbf{x} is the vector containing the diagonal elements. The function $\log(\cdot)$ represents the natural logarithm, and \mathbf{I}_m signifies the identity matrix of size $m \times m$.

This article's structure is given as follows. In Section II, we introduce a novel algorithm, RW-MM, for addressing the R-WLS problem using the MM framework. Section III is dedicated to developing a localization technique that accounts for measurement errors, clock bias, and gNB position errors. Section IV discusses optimal UE placement. The simulation results of the localization process can be found in Section V. To conclude, Section VI summarizes the key findings of this study.

II. PROBLEM FORMULATION

The assessment of error statistics is conducted in the presence of multipath conditions. In this article, the positioning signals utilized are obtained from the downlink signals within the 5G network. Additionally, our study focuses on a single-user positioning scenario in a 5G environment with 5G applications like autonomous driving. The channel impulse response (CIR) is simulated using ray-tracing, as described in [23]. The orthogonal frequency division multiplexing (OFDM) symbol is transmitted in a multipath fading channel, which is assumed to stay constant over the duration of a symbol and has the CIR as

$$h(\tau) = \sum_{l=0}^{L-1} \alpha_l \delta(\tau - \tau_l) \quad (1)$$

where L represents the count of multipath components, α_l , and τ_l denote the relative attenuation and delay components of the l th path concerning the first path.

In the process of localization, gNBs capture TOA measurements of the UE signal by analyzing specific signal features, such as preambles transmitted by the UE. To be precise, we have a set of known coordinates for the i th gNB, denoted as $\mathbf{t}_i \in \mathbb{R}^n$, and an unknown UE coordinate vector $\mathbf{r} \in \mathbb{R}^n$. Let c be the velocity of electromagnetic waves, the unknown vector is defined as $\mathbf{x} = [\mathbf{r}, c \cdot (\delta t_{\text{UE}} - \delta t_{\text{gNB}})]^T$, where δt_{UE} and δt_{gNB} are the UE's and the i th gNB's clock biases, respectively. To be more specific, given an LOS propagation path, the noisy range measurement $\hat{\rho}_i$ is described as

$$\begin{aligned} \hat{\rho}_i &= \|\mathbf{r} - \mathbf{t}_i\| + c \cdot (\delta t_{\text{UE}} - \delta t_{\text{gNB}}) + v_i \\ &\triangleq \rho_i + v_i, i = 1, \dots, N \end{aligned} \quad (2)$$

where v_i is the TOA measurement error, which follows a zero-mean independent Gaussian noise with variance σ_i^2 . For convenience, let the term $c \cdot (\delta t_{\text{UE}} - \delta t_{\text{gNB}})$ be b .

In the context of 5G systems, concerning the OFDM signal, the variance¹ of v_i can be calculated by

$$\sigma_i^2 = \text{var}(v_i) = \frac{c^2 T_s^2}{8\pi^2 \cdot \text{SNR}_i \cdot \sum_{n \in \mathcal{N}_{\text{PRS}}} p_n^2 \cdot n^2} \quad (3)$$

where T_s represents the OFDM symbol duration, SNR_i represents the SNR at the i th gNB, \mathcal{N}_{PRS} refers to the subset of subcarriers dedicated to the positioning reference signal (PRS), while p_n^2 signifies the relative power weight assigned to the n th subcarrier.

¹According to [24], (3) is obtained from the CRLB of the time delay estimation.

In TOA-based UE localization, the main objective is to estimate the UE's position based on given noisy TOA measurements. This estimation is commonly achieved through a weighted least-squares approach, which mathematically aims to minimize the sum of squared errors

$$\min_{\mathbf{r}, b} f_{\text{R-WLS}}(\mathbf{r}, b) = \sum_{i=1}^N \frac{(\hat{\rho}_i - \|\mathbf{r} - \mathbf{t}_i\| - b)^2}{\sigma_i^2}. \quad (4)$$

On expanding $f_{\text{R-WLS}}(\mathbf{r}, b)$ we get

$$\begin{aligned} \min_{\mathbf{r}, b} f_{\text{R-WLS}}(\mathbf{r}, b) &\triangleq \\ \sum_{i=1}^N \frac{\rho_i^2 + \|\mathbf{r} - \mathbf{t}_i\|^2 + b^2 - 2\hat{\rho}_i\|\mathbf{r} - \mathbf{t}_i\| - 2\hat{\rho}_i b + 2b\|\mathbf{r} - \mathbf{t}_i\|}{\sigma_i^2}. \end{aligned} \quad (5)$$

III. RW-MM ALGORITHM FOR 5G LOCALIZATION PROBLEM

In this section, we first propose an efficient RW-MM algorithm for the problem (4) based on the MM. The method we proposed holds promise for application in various localization scenarios, including but not limited to autonomous driving. This suggests its adaptability and relevance in addressing the complex positioning requirements of emerging technologies and industries. We then analyze convergence of the RW-MM algorithm and demonstrate that the proposed algorithm converges to a stationary point. Note that the objective function described above contains two challenging components. First, there is the term $-2\hat{\rho}_i\|\mathbf{r} - \mathbf{t}_i\|$, which is both nonsmooth and nonconvex. Second, the term $b\|\mathbf{r} - \mathbf{t}_i\|$ is coupled, further complicating the solution of the R-WLS problem.

A. MM Framework

The MM framework utilizes the problem's inherent structure to create a customized algorithm, and it follows a two-step process. In the first step, majorization is employed to create a surrogate function that globally approximates the objective function, while minimizing the gap between them at the current point. The second step is centered on minimization, where the surrogate function from the previous step is systematically minimized to reach its minimum value.

Let us consider the following minimization optimization problem:

$$\begin{aligned} \min_{\mathbf{x}} \quad & \phi(\mathbf{x}) \\ \text{s.t.} \quad & \mathbf{x} \in \chi \end{aligned} \quad (6)$$

where χ is a nonempty closed set. The MM method starts with the initialization of a point \mathbf{x}_0 within the set χ , assuming that $\phi(\mathbf{x})$ goes to infinity as $\|\mathbf{x}\|_2 \rightarrow +\infty$. Subsequently, a sequence of feasible points \mathbf{x}_t is iteratively generated. In the initial stage, a surrogate function $t(\mathbf{x}|\mathbf{x}_t)$ is created at \mathbf{x}_t with the following properties:

$$t(\mathbf{x}|\mathbf{x}_t) \geq \phi(\mathbf{x}) + d_t \quad \forall \mathbf{x} \in \chi \quad (7)$$

where $d_t = t(\mathbf{x}_t|\mathbf{x}_t) - \phi(\mathbf{x}_t)$. The difference of $t(\cdot|\mathbf{x}_t)$ and ϕ is minimized at the point \mathbf{x}_t . In the subsequent minimization

step, the update of \mathbf{x} occurs, and this takes place during the second phase of the process

$$\mathbf{x}_{t+1} = \arg \min_{\mathbf{x} \in \chi} t(\mathbf{x} | \mathbf{x}_t). \quad (8)$$

From (7) and (8), we have the following inequality:

$$\phi(\mathbf{x}_{t+1}) \leq t(\mathbf{x}_{t+1} | \mathbf{x}_t) \leq t(\mathbf{x}_t | \mathbf{x}_t) = \phi(\mathbf{x}_t). \quad (9)$$

The presented process establishes a sequence $(\phi(\mathbf{x}_t))$ that monotonically decreases, signifying a consistent reduction in the objective function through the MM technique [25]. The effectiveness of the MM technique relies heavily on creating a suitable surrogate function. Designing a surrogate function that is not only smooth and convex but also amenable to variable separation is crucial. These attributes facilitate efficient and scalable minimization, resulting in easily implementable algorithms. However, there is a delicate balance to be struck when crafting a surrogate function. It entails finding the right tradeoff between achieving rapid convergence and maintaining minimal computational complexity and memory usage per iteration. Striking this balance is vital for the successful application of the MM approach. This intricate interplay ensures that the surrogate function closely approximates the shape of the objective function, expediting convergence while keeping minimization manageable in terms of computational demands.

B. 5G Localization via Iterative MM Technique

Introducing RW-MM, an iterative algorithm designed to address the R-WLS problem using the MM approach. The terms within $f_{R-WLS}(\mathbf{r}, b)$, including both norm and cross terms, lack continuous differentiability. Consequently, obtaining a closed-form solution for the R-WLS problem based on first-order conditions is a challenging task. To overcome this, we introduce a surrogate function, $t(\mathbf{x} | \mathbf{x}_t)$, to provide a majorization of these nondifferentiable terms, effectively majorizing $f_{R-WLS}(\mathbf{r}, b)$, in accordance with the following lemmas [25].

Lemma 1: Given any $\mathbf{r} = \mathbf{r}_t$, $-\|\mathbf{r} - \mathbf{t}_i\|_2$ can be upper bounded given by

$$-\|\mathbf{r} - \mathbf{t}_i\|_2 \leq -\frac{(\mathbf{r} - \mathbf{t}_i)^T (\mathbf{r}_t - \mathbf{t}_i)}{\|\mathbf{r}_t - \mathbf{t}_i\|_2}. \quad (10)$$

The upper bound for $-\|\mathbf{r} - \mathbf{t}_i\|_2$ exhibits linearity and differentiability concerning \mathbf{r} .

In order to derive a separable surrogate function, it is essential to address the cross terms involving $b\|\mathbf{r} - \mathbf{t}_i\|$ by applying the following Lemma.

Lemma 2: Let m and n denotes two nonnegative scalar variables, then given some m_t and n_t , the term mn can be upper bounded as follows:

$$mn \leq \frac{1}{2} \left(\frac{m_t}{n_t} n^2 + \frac{n_t}{m_t} m^2 \right). \quad (11)$$

Given some $b = b_t$ and $\mathbf{r} = \mathbf{r}_t$, we have

$$b\|\mathbf{r} - \mathbf{t}_i\| \leq \frac{1}{2} \left(\frac{b_t}{\|\mathbf{r}_t - \mathbf{t}_i\|} \|\mathbf{r} - \mathbf{t}_i\|^2 + \frac{\|\mathbf{r}_t - \mathbf{t}_i\|}{b_t} b^2 \right). \quad (12)$$

Using Lemmas 1 and 2, we arrive at the surrogate function (13), which is presented at the bottom of the following page.

Note that for all \mathbf{r}, b , the inequality $t(\mathbf{r}, b | \mathbf{r}_t, b_t) \geq f_{R-WLS}(\mathbf{r}, b)$ holds, with equality being achieved when $\mathbf{r} = \mathbf{r}_t$ and $b = b_t$. The surrogate function in (13) is convex, thanks to its separability in \mathbf{r}, b , where the terms involved are either quadratic or linear functions of (\mathbf{r}, b) . Additionally, this function is differentiable concerning \mathbf{r} and b .

Therefore, in any given iteration with the values of \mathbf{r}_t and b_t specified, the surrogate function minimization problem for (4) can be expressed as

$$\min_{\mathbf{r}} t(\mathbf{r}, b | \mathbf{r}_t, b_t). \quad (14)$$

Consequently, we attain the optimal solution for \mathbf{r}, b , which will serve as the next iteration, and the problem described above has a closed-form minimizer, given by

$$\mathbf{r}_{t+1} = \frac{\sum_{i=1}^N \left(\frac{t_i s_i + \hat{\rho}_i (\mathbf{r}_t - \mathbf{t}_i)}{q_i} \right)}{\sum_{i=1}^N \frac{s_i}{q_i}}, \quad (15)$$

$$b_{t+1} = \frac{\sum_{i=1}^N \sigma_i^{-2} \hat{\rho}_i}{\sum_{i=1}^N \frac{s_i}{b_i \sigma_i^2}} \quad (16)$$

where $s_i = \|\mathbf{r}_t - \mathbf{t}_i\|_2 + b$, $q_i = \sigma_i^2 \|\mathbf{r}_t - \mathbf{t}_i\|_2$.

C. Convergence Proof of the RW-MM Algorithm

Given that the proposed RW-MM algorithm is rooted in the MM method, it guarantees that the sequence of points $\{\mathbf{x}_t\}$ consistently reduces the R-WLS problem. Furthermore, the R-WLS problem is constrained to have a lower bound of zero. Consequently, the sequence $f_{R-WLS}(\mathbf{x})$ generated by the proposed algorithm will, at the very least, converge to a finite value. In the following discussion, we illustrate that the RW-MM algorithm guarantees convergence under the condition that the surrogate function $t(\cdot, \cdot)$ satisfies specific assumptions, which we will detail shortly.

Assumption 1: Assume that the surrogate function $t(\cdot, \cdot)$ adheres to the following conditions:

$$t(\mathbf{y}, \mathbf{y}) = f(\mathbf{y}) \quad \forall \mathbf{y} \in \chi \quad (17a)$$

$$t(\mathbf{x}, \mathbf{y}) \geq f(\mathbf{x}) \quad \forall \mathbf{x}, \mathbf{y} \in \chi \quad (17b)$$

$$\nabla t(\mathbf{x} | \mathbf{y}; \mathbf{d})|_{\mathbf{x}=\mathbf{y}} = \nabla f(\mathbf{y}; \mathbf{d}) \quad \forall \mathbf{d} \text{ with } \mathbf{y} + \mathbf{d} \in \chi \quad (17c)$$

$$t(\mathbf{x}, \mathbf{y}) \text{ is a continuous function in } (\mathbf{x}, \mathbf{y}). \quad (17d)$$

The assumptions (17a) and (17b) indicate that the surrogate function $t(\cdot, \mathbf{x}_{t-1})$ acts as a strict upper bound for the original

$$t(\mathbf{r}, b | \mathbf{r}_t, b_t) = \sum_{i=1}^N \frac{\rho_i^2 + b^2 - 2\hat{\rho}_i b + \|\mathbf{r} - \mathbf{t}_i\|^2 - \frac{2\hat{\rho}_i (\mathbf{r} - \mathbf{t}_i)^T (\mathbf{r}_t - \mathbf{t}_i)}{\|\mathbf{r}_t - \mathbf{t}_i\|_2} + \frac{b_t}{\|\mathbf{r}_t - \mathbf{t}_i\|} \|\mathbf{r} - \mathbf{t}_i\|^2 + \frac{\|\mathbf{r}_t - \mathbf{t}_i\|}{b_t} b^2}{\sigma_i^2}. \quad (13)$$

problem. Assumption (17d) requires that the surrogate function $t(\mathbf{x}, \mathbf{y})$ should exhibit joint continuity in both variables, \mathbf{x} and \mathbf{y} . Furthermore, assumption (17c) ensures that the first-order behavior of $t(\cdot, \mathbf{x}_{t-1})$ locally aligns with that of $f(\cdot)$ (noting that the directional derivative $\nabla t(\mathbf{x}|\mathbf{y}; \mathbf{d})$ pertains exclusively to the variable \mathbf{x} in the direction \mathbf{d}) [26]. As previously mentioned, the surrogate function in (13) is convex due to its separability in \mathbf{r} and b , where the terms involved are either quadratic or linear functions of (\mathbf{r}, b) . Moreover, this function is differentiable with respect to \mathbf{r} and b . Therefore, all assumptions are met for the surrogate function in (13).

We then prove that the sequence $\{\mathbf{x}_t\}$ points will converge to a stationary point. The subsequent theorem establishes the convergence of the RW-MM algorithm.

Theorem 1: If Assumption 1 is met, then any limit point obtained from the iterations produced by the RW-MM algorithm qualifies as a stationary point of the problem (4).

Proof: A point \mathbf{x} is considered stationary when it satisfies the following:

$$\nabla f_{\text{R-WLS}}(\mathbf{x}; \mathbf{d}) \geq 0 \quad (18)$$

where ∇ is the directional derivative of the original function, $f_{\text{R-WLS}}(\cdot)$ at point \mathbf{x} and is defined as

$$\nabla f_{\text{R-WLS}}(\mathbf{x}; \mathbf{d}) = \liminf_{\Delta \rightarrow 0} \frac{f_{\text{R-WLS}}(\mathbf{x} + \Delta \mathbf{d}) - f_{\text{R-WLS}}(\mathbf{x})}{\Delta}. \quad (19)$$

A straightforward implication of (9) is that the sequence of objective function values does not increase, which means that

$$f_{\text{R-WLS}}(\mathbf{x}^0) \geq f_{\text{R-WLS}}(\mathbf{x}^1) \geq f_{\text{R-WLS}}(\mathbf{x}^2) \dots \quad (20)$$

Suppose that there exists a subsequence \mathbf{x}^{r_j} that converges to a limit point \mathbf{z} . In this case, (17a) and (17b), along with (20), imply that

$$\begin{aligned} t(\mathbf{x}^{r_{j+1}} | \mathbf{x}^{r_{j+1}}) &= f_{\text{R-WLS}}(\mathbf{x}^{r_{j+1}}) \leq f_{\text{R-WLS}}(\mathbf{x}^{r_{j+1}}) \\ &\leq t(\mathbf{x}^{r_{j+1}} | \mathbf{x}^{r_j}) \leq t(\mathbf{x} | \mathbf{x}^{r_j}). \end{aligned} \quad (21)$$

Letting $j \rightarrow \infty$, we obtain

$$t(\mathbf{z} | \mathbf{z}) \leq t(\mathbf{x} | \mathbf{z}) \quad (22)$$

which implies that $\nabla t(\mathbf{x} | \mathbf{z}; \mathbf{d})_{\mathbf{x}=\mathbf{z}} \geq 0$, and $\nabla f(\mathbf{z}; \mathbf{d}) \geq 0$. Consequently, \mathbf{z} is a stationary point of $f_{\text{R-WLS}}(\cdot)$, and as a result, the proposed RW-MM algorithm converges to a stationary point of $f_{\text{R-WLS}}(\mathbf{x})$. ■

D. Performance Evaluation

In the following, we conduct a comprehensive examination of the proposed method, with a primary focus on evaluating the objective function $f_{\text{R-WLS}}(\mathbf{x})$. We will perform a comparative analysis against $f_{\text{R-WLS}}(\mathbf{x})$, providing valuable insights into the relative effectiveness of our approach. Furthermore, we will delve into the concept of majorization in the context of $f_{\text{R-WLS}}(\mathbf{x})$, demonstrating how this technique can be effectively applied. However, the optimal scenario involves crafting a surrogate function that faithfully mimics the characteristics of the original objective function. This alignment between the

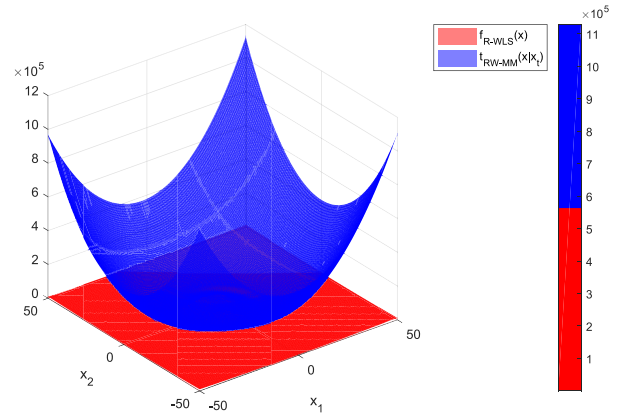


Fig. 1. Surrogate function of RW-MM majorizes the objective function $f_{\text{R-WLS}}$ at the point $\mathbf{x}_t = (x_t^1, x_t^2)$.

Algorithm 1 Pseudocode of the RW-MM Algorithm

- 1: **Input:** gNB positions $(t_1, t_2 \dots t_N)$, measurement noise $(v_1, v_2 \dots v_N)$
- 2: **Output:** \mathbf{r}, b
- 3: Initialization: Initialize $\mathbf{r}_0, b_0, t = 0$
- 4: **while** $\|\mathbf{r}_{t+1} - \mathbf{r}_t\| / \|\mathbf{r}_t\| \leq \epsilon$ **do**
- 5: Compute s_i, q_i
- 6: Compute \mathbf{r} from (15)
- 7: Solve (16) to obtain b
- 8: $\mathbf{r}_{t+1} = \mathbf{r}, b_{t+1} = b, t \leftarrow t + 1$
- 9: **end while**

two functions significantly impacts the convergence rate of the algorithm. We plot the surrogate functions of RW-MM for $n = 2$ and $N = 4$ in Fig. 1. Fig. 1 shows the value taken by the objective function and the surrogate function for various values of $\mathbf{x} = [x^1, x^2, b]^T$ with $b = 0.1$. Pseudocode to update \mathbf{x} via RW-MM algorithm is given in Algorithm 1.

IV. PRESENCE OF GNB POSITION ERROR

In this section, we derive a localization technique considering the coexistence of measurement errors, clock bias, and gNB position errors. We introduce a robust weighted semidefinite relaxation (SDR) method that accounts for individual gNB position errors. Additionally, we conduct an analysis of the computational complexity associated with various TOA-based UE localization algorithms.

In the previously mentioned WLS formulation, the assumption is that the gNB positions are precisely known. However, obtaining accurate position estimates for a set of N gNBs can be quite challenging, especially in situations where GNSS signals are not available. Therefore, we introduce gNB position errors into our model to better represent the UE localization process. In this context, the position of the i th gNB can be written as $\tilde{\mathbf{t}}_i = \mathbf{t}_i + \boldsymbol{\xi}_i$, where $\boldsymbol{\xi}_i \in \mathbb{R}^n$ represents the position estimation error.

The conventional robust LS estimator operates under the assumption that gNB position errors conform to a Gaussian distribution. Nonetheless, the efficacy of localization is

significantly contingent on the accuracy of modeling the error distribution. It is apparent that the Gaussian distribution assumption falls short under conditions marked by environment-specific and dynamic variations. In response to these complexities, we abstain from imposing a specific probability distribution on ξ_i and, instead, prioritize establishing an upper-bound constraint.

A. 5G Localization via Robust Semidefinite Relaxation

In this section, we introduce a novel approach that simultaneously addresses the estimation of both the UE position and the clock bias under gNB position error condition. Furthermore, our methodology is designed to enhance robustness against gNB position errors. Specifically, we establish that the estimation error of the i th gNB, ξ_i , is confined within a predefined threshold, denoted as $\|\xi_i\| \leq \varepsilon$. The first-order Taylor expansion to on $\|\mathbf{r} - \tilde{\mathbf{t}}_i\|$ on $\tilde{\mathbf{t}}_i$ can be expressed as

$$\|\mathbf{r} - \mathbf{t}_i\| \approx \|\mathbf{r} - \tilde{\mathbf{t}}_i\| - \frac{\xi_i^T(\mathbf{r} - \tilde{\mathbf{t}}_i)}{\|\mathbf{r} - \tilde{\mathbf{t}}_i\|} + o(\|\xi_i^T\|). \quad (23)$$

For convenience, we define $\tilde{a}_i = \|\mathbf{r} - \tilde{\mathbf{t}}_i\|$, $\epsilon_i = -([\xi_i^T(\mathbf{r} - \tilde{\mathbf{t}}_i)]/[\|\mathbf{r} - \tilde{\mathbf{t}}_i\|])$. Then, we have the following inequality:

$$|\epsilon_i|^2 = \frac{\xi_i^T \tilde{a}_i \xi_i^T \tilde{a}_i}{\|\tilde{a}_i\|^2} \leq \frac{\xi_i^T \xi_i (\tilde{a}_i)^T (\tilde{a}_i)}{\|\tilde{a}_i\|^2} = \xi_i^T \xi_i = \delta^2. \quad (24)$$

The TOA measurements $\hat{\rho}_i$ at gNB $\tilde{\mathbf{t}}_i$ can be written as

$$\hat{\rho}_i = \tilde{a}_i + b + \epsilon_i + v_i + o(\|\xi_i^T\|), i = 1, 2, \dots, N. \quad (25)$$

WLS poses a challenging nonconvex problem. To make it more manageable, we employ the S-Lemma to transform the nonconvex R-WLS problem into a solvable SDP. We formulate the nonconvex R-WLS problem as a *worst-case* robust optimization problem

$$\begin{aligned} & \min_{\mathbf{r}, \{\tilde{a}_i\}, b} \max_{|\epsilon_i|^2 \leq \delta} \sum_{i=1}^N \frac{(\hat{\rho}_i - \tilde{a}_i - \epsilon_i - b)^2}{\sigma_i^2} \\ & \text{s.t. } \tilde{a}_i = \|\mathbf{r} - \tilde{\mathbf{t}}_i\|, i = 1, 2, \dots, N. \end{aligned} \quad (26)$$

Let $g_i = \hat{\rho}_i - \tilde{a}_i - b$, we have

$$\sum_{i=1}^N \frac{(g_i - \epsilon_i)^2}{\sigma_i^2} = \sum_{i=1}^N \frac{g_i^2 - 2g_i\epsilon_i + \epsilon_i^2}{\sigma_i^2}. \quad (27)$$

The problem described in (26) can be reformulated in the epigraph form as follows:

$$\begin{aligned} & \min_{\mathbf{r}, \{\tilde{a}_i\}, b, \{\tau_i\}} \sum_{i=1}^N \tau_i \end{aligned} \quad (28)$$

$$\text{s.t. } \tilde{a}_i = \|\mathbf{r} - \tilde{\mathbf{t}}_i\| \quad (28a)$$

$$\max_{|\epsilon_i| \leq \delta} \frac{g_i^2 - 2g_i\epsilon_i + \epsilon_i^2}{\sigma_i^2} \leq \tau_i \quad (28b)$$

$$g_i = \hat{\rho}_i - \tilde{a}_i - b, i = 1, 2, \dots, N. \quad (28c)$$

Furthermore, we can deduce the following scalar inequalities by utilizing the implication form:

$$|\epsilon_i| \leq \delta \Rightarrow \frac{g_i^2 - 2g_i\epsilon_i + \epsilon_i^2}{\sigma_i^2} \leq \tau_i. \quad (29)$$

By defining $\mathbf{g} = [g_1, \dots, g_N]^T$ and $\mathbf{G} = \mathbf{g}\mathbf{g}^T$, we have

$$[\mathbf{G}]_{ii} = g_i^2 = (\hat{\rho}_i - \tilde{a}_i - b)^2, \frac{[\mathbf{G}]_{ii} - 2g_i\epsilon_i + \epsilon_i^2}{\sigma_i^2} \leq \tau_i. \quad (30)$$

The inequality of (30) can be further reformed as

$$\begin{bmatrix} \epsilon_i \\ 1 \end{bmatrix}^T \begin{pmatrix} 1 & \frac{g_i}{\sigma_i^2} \\ \frac{g_i}{\sigma_i^2} & \frac{[\mathbf{G}]_{ii}}{\sigma_i^2} - \tau_i \end{pmatrix} \begin{bmatrix} \epsilon_i \\ 1 \end{bmatrix} \leq 0. \quad (31)$$

Utilizing S-Lemma, we can deduce from the equation above that there exists a $\lambda_i \geq 0$ such that

$$\begin{pmatrix} 1 & \frac{g_i}{\sigma_i^2} \\ \frac{g_i}{\sigma_i^2} & \frac{[\mathbf{G}]_{ii}}{\sigma_i^2} - \tau_i \end{pmatrix} \preceq \lambda_i \begin{pmatrix} 1 & 0 \\ 0 & -\delta^2 \end{pmatrix} \quad (32)$$

i.e.,

$$\begin{bmatrix} \lambda_i - 1 & -\frac{g_i}{\sigma_i^2} \\ -\frac{g_i}{\sigma_i^2} & -\lambda_i \delta^2 - \frac{[\mathbf{G}]_{ii}}{\sigma_i^2} + \tau_i \end{bmatrix} \succeq 0. \quad (33)$$

Thus, problem (28) can be equivalently written as

$$\begin{aligned} & \min_{\mathbf{r}, \{\tilde{a}_i\}, b, \{\mathbf{G}\}, \{\tau_i\}} \sum_{i=1}^N \tau_i \end{aligned} \quad (34)$$

s.t. (28a)

$$g_i = \rho_i - \tilde{a}_i - b \quad (34a)$$

$$\mathbf{G} = \mathbf{g}\mathbf{g}^T \quad (34b)$$

$$\begin{bmatrix} \lambda_i - 1 & -\frac{g_i}{\sigma_i^2} \\ -\frac{g_i}{\sigma_i^2} & -\lambda_i \delta^2 - \frac{[\mathbf{G}]_{ii}}{\sigma_i^2} + \tau_i \end{bmatrix} \succeq 0 \quad (34c)$$

$$\lambda_i \geq 0, \quad \tau_i \geq 0, \quad i = 1, 2, \dots, N. \quad (34d)$$

Even though the maximization component in the original problem (28) has been removed, it is important to note that problem (34) remains a nonconvex problem. By defining $\boldsymbol{\rho} = [\rho_1, \dots, \rho_N]^T$, $\mathbf{b} = [b, \dots, b]^T$ and $\mathbf{a} = [a_1, \dots, a_N]^T$, we have

$$\mathbf{G} = \mathbf{g}\mathbf{g}^T = (\boldsymbol{\rho} - \tilde{\mathbf{a}} - \mathbf{b})(\boldsymbol{\rho} - \tilde{\mathbf{a}} - \mathbf{b})^T. \quad (35)$$

Let $\mathbf{Bh} \triangleq \tilde{\mathbf{a}} + \mathbf{b}$, where $\mathbf{B} \triangleq [\mathbf{I}_N, \mathbf{1}_N]$, and $\mathbf{h} \triangleq [a_1, \dots, a_N, b]^T$, we obtain the following expression:

$$\mathbf{G} = (\boldsymbol{\rho} - \mathbf{Bh})(\boldsymbol{\rho} - \mathbf{Bh})^T = \boldsymbol{\rho}\boldsymbol{\rho}^T - 2\mathbf{Bh}\mathbf{d}^T + \mathbf{BCB}^T \quad (36)$$

where $\mathbf{C} \triangleq \mathbf{h}\mathbf{h}^T$. Note that the diagonal elements of the matrix \mathbf{C} satisfy the following conditions:

$$\begin{aligned} [\mathbf{C}]_{ii} &= (\mathbf{r} - \tilde{\mathbf{t}}_i)^T (\mathbf{r} - \tilde{\mathbf{t}}_i) \\ &= \mathbf{r}^T \mathbf{r} - 2\tilde{\mathbf{t}}_i^T \mathbf{r} + \tilde{\mathbf{t}}_i^T \tilde{\mathbf{t}}_i \\ &= y - 2\tilde{\mathbf{t}}_i^T \mathbf{r} + \tilde{\mathbf{t}}_i^T \tilde{\mathbf{t}}_i, \quad i = 1, 2, \dots, N \end{aligned} \quad (37)$$

where $y = \mathbf{r}^T \mathbf{r}$. Equation (37) can be alternatively written as

$$[\mathbf{C}]_{ii} = \begin{bmatrix} \tilde{\mathbf{t}}_i \\ -1 \end{bmatrix}^T \begin{pmatrix} \mathbf{I} & \mathbf{r} \\ \mathbf{r}^T & y \end{pmatrix} \begin{bmatrix} \tilde{\mathbf{t}}_i \\ -1 \end{bmatrix}, \quad i = 1, 2, \dots, N. \quad (38)$$

By relaxing the conditions $\mathbf{G} = \mathbf{g}\mathbf{g}^T$, $\mathbf{C} = \mathbf{h}\mathbf{h}^T$, and $y = \mathbf{r}^T \mathbf{r}$, then dropping the rank one constraint, we can transform the problem into a convex SDP. This leads to the following equivalence:

$$\begin{pmatrix} \mathbf{G} & \mathbf{g} \\ \mathbf{g}^T & 1 \end{pmatrix} \succeq 0, \begin{pmatrix} y & \mathbf{r} \\ \mathbf{r}^T & \mathbf{I} \end{pmatrix} \succeq 0, \begin{pmatrix} \mathbf{C} & \mathbf{h} \\ \mathbf{h}^T & 1 \end{pmatrix} \succeq 0. \quad (39)$$

To tighten the relaxed problem (34a), we introduce additional constraints by employing the Cauchy–Schwarz inequality, as follows:

$$\begin{aligned} [\mathbf{C}]_{ij} &= \|\mathbf{r} - \tilde{\mathbf{t}}_i\| \|\mathbf{r} - \tilde{\mathbf{t}}_j\| \\ &\geq \begin{bmatrix} \tilde{\mathbf{t}}_i \\ -1 \end{bmatrix}^T \begin{pmatrix} \mathbf{I} & \mathbf{r} \\ \mathbf{r}^T & y \end{pmatrix} \begin{bmatrix} \tilde{\mathbf{t}}_j \\ -1 \end{bmatrix}, \quad i, j = 1, 2, \dots, N, i < j. \end{aligned} \quad (40)$$

To enhance problem tightness, we incorporate additional constraints into the optimization problem

$$\begin{aligned} \|\mathbf{r} - \tilde{\mathbf{t}}_i\| &\leq h_i, \quad i = 1, 2, \dots, N \\ [\mathbf{C}]_{N+1,N+1} &\geq 0. \end{aligned} \quad (41)$$

By including the constraints in (39)–(41) into problem (34), we arrive at the following SDP:

$$\begin{aligned} \min_{\substack{\mathbf{r}, \mathbf{G}, b, y, \mathbf{g}, \\ \mathbf{C}, \mathbf{h}, \{\lambda_i\}, \{\tau_i\}}} \quad & \sum_{i=1}^N \tau_i \\ \text{s.t. } & (34c), (34d), (39), (40), (41). \end{aligned} \quad (42)$$

The convex optimization problem presented in (42) can be efficiently tackled using interior point methods. In this article, we employ a well-known CVX tool to numerically address the problem in the simulations.

B. Impact of Constraints Associated With gNB Position Errors

1) Lower Bound of Objective Function: The method described above highlights that the constraints related to gNB position errors are solely encapsulated by (33), in conjunction with the variables τ_i integrated into the objective function, creating a robust convex optimization formulation. An aspect to consider is how the specific constraints of gNB position errors within (33) and the scale λ_i impact the convex optimization problem.

Theorem 2: Given the constraints related to the gNB position error (33), the function can be lower bounded by

$$\tau_i \geq \lambda_i \delta^2 + \frac{\sigma_i^2(\lambda_i - 1) + 1}{\sigma_i^4(\lambda_i - 1)} (\hat{\rho}_i - \tilde{a}_i - b)^2, \quad i = 1, \dots, N. \quad (43)$$

Proof: In order for the matrix

$$\begin{bmatrix} \lambda_i - 1 & -\frac{g_i}{\sigma_i^2} \\ -\frac{g_i}{\sigma_i^2} & -\lambda_i \delta^2 - \frac{[\mathbf{G}]_{ii}}{\sigma_i^2} + \tau_i \end{bmatrix} \quad (44)$$

to be positive semidefinite, the value of the scale λ_i needs to satisfy the following conditions. A matrix is positive semidefinite if and only if all of its eigenvalues are nonnegative. Therefore, the determinant $(\lambda_i - 1)(-\lambda_i \delta^2 - ([\mathbf{G}]_{ii}/\sigma_i^2) + \tau_i) - (g_i/\sigma_i^2)^2$ of the matrix is nonnegative, which means $\lambda_i - 1 \geq 0$ and $-\lambda_i \delta^2 - ([\mathbf{G}]_{ii}/\sigma_i^2) + \tau_i \geq 0$. Using $\lambda_i \neq 1$, we have $\lambda_i - 1 > 0$ and obtain

$$(\lambda_i - 1) \left(-\lambda_i \delta^2 - \frac{[\mathbf{G}]_{ii}}{\sigma_i^2} + \tau_i \right) - \left(\frac{g_i}{\sigma_i^2} \right)^2 \geq 0 \quad (45)$$

which can be equivalently written as

$$\tau_i \geq \lambda_i \delta^2 + \frac{[\mathbf{G}]_{ii}}{\sigma_i^2} + \frac{g_i^2}{\sigma_i^4(\lambda_i - 1)}. \quad (46)$$

After substituting $[\mathbf{G}]_{ii} = g_i^2 = (\hat{\rho}_i - \tilde{a}_i - b)^2$, the above inequality can be compactly rewritten as

$$\tau_i \geq \lambda_i \delta^2 + \frac{\sigma_i^2(\lambda_i - 1) + 1}{\sigma_i^4(\lambda_i - 1)} (\hat{\rho}_i - \tilde{a}_i - b)^2, \quad i = 1, \dots, N. \quad \blacksquare$$

Clearly, the function linked to the gNB position error incorporates a lower-bound constraint. This lower bound can be interpreted as a weighted least squares term.

2) Possible Optimal Scale of λ :

Corollary 1: Given that

$$\tau_i \geq g(\lambda_i) \triangleq \lambda_i \delta^2 + \frac{g_i^2}{\sigma_i^2} + \frac{g_i^2}{\sigma_i^4(\lambda_i - 1)} \quad (47)$$

this lower bound of $g(\lambda_i)$ is attained when

$$\lambda_i = \frac{|g_i|}{\delta \sigma_i^2} + 1, \quad i = 1, \dots, N. \quad (48)$$

Proof: Considering $g_i = \hat{\rho}_i - \tilde{a}_i - b$, we have

$$\tau_i \geq g(\lambda_i) \triangleq \lambda_i \delta^2 + \frac{g_i^2}{\sigma_i^2} + \frac{g_i^2}{\sigma_i^4(\lambda_i - 1)}.$$

To find a minimizer of the function, we set the gradient of $g(\lambda_i)$ with respect to λ_i ($\lambda_i - 1 > 0$) to zero, which leads to the minimizer

$$\lambda_i = \frac{|g_i|}{\delta \sigma_i^2} + 1, \quad i = 1, \dots, N. \quad \blacksquare$$

Corollary 2: Given that the constraint $|\epsilon_i| \leq \delta$, we arrive at the following scale-bounded constraint given by:

$$1 < \lambda_i \leq \frac{1}{\sigma_i^2} + 1, \quad i = 1, \dots, N. \quad (49)$$

Proof: By neglecting the high-order terms in (25), the term g_i is primarily composed of two sources of errors: 1) gNB position error and 2) measurement noise. In cases where the gNB position is obtained from GNSS, it is often observed that the gNB position error significantly outweighs the measurement noise, meaning that $\epsilon_i \gg v_i$ in 5G environments. Consequently, we arrive at

$$\lambda_i \approx \frac{|\epsilon_i|}{\delta \sigma_i^2} + 1. \quad (50)$$

Considering the constraint $|\epsilon_i| \leq \delta$, it follows that:

$$1 < \lambda_i \leq \frac{1}{\sigma_i^2} + 1, i = 1, \dots, N.$$

■

It is noteworthy that Corollary 2 presents an optimal value for the scale λ_i in scenarios where the objective function exhibits a lower bound.

C. Computational Complexity Analysis

The computational complexity of the proposed RRW-SDR method, scales on the order of $\mathcal{O}(N^{6.5})$ [27]. This complexity level is comparable to that of the robust SDP method [11]. Although the complexity of the proposed RRW-SDR method surpasses that of the other methods, it can be mitigated by exploiting the inherent structure of the data matrix. Furthermore, especially for TOA-based localization systems, where the gNB count is usually small, the proposed method remains viable for efficient real-time implementation. Moreover, our paper demonstrates that the proposed SDR approach outperforms alternative methods. Although the RRW-SDR method may face challenges regarding computational efficiency and real-time performance, its capability to effectively manage BS location uncertainty makes it a valuable asset for post-processing in practical 5G positioning applications.

V. OPTIMAL GEOMETRY ANALYSIS

In this context, we employ the CRLB to construct an error ellipse, which describes the spatial distribution of variance in UE estimation. Both the CRLB and the error ellipse are influenced by the geometric relationship between the gNBs and the UE.

The optimization of the gNB-UE geometric configuration aligns with the principles of experimental design theory [28]. For example, the concept of *A-optimality* (trace) aims to minimize the trace of the inverse of the FIM, leading to decreased average variance in UE state estimates. On the other hand, D-optimality (determinant) seeks to maximize the determinant of the FIM, thereby minimizing the volume of the errors ellipsoid around the UE state estimates. Notably, D-optimality maintains its characteristics under changes in parameter scale and linear transformations of the output, whereas A-optimality is influenced by these transformations.

A. CRLB

In order to achieve a highly accurate estimation of the UE position, we strive to optimize the gNB geometry. The precision of this estimation can be quantified by determining the minimum possible estimation error, which can be obtained from the CRLB matrix. The CRLB matrix is derived from the inverse of the FIM. Specifically, when estimating the parameter vector \mathbf{x} from the measurement vector ρ , the FIM is given by the following expression:

$$\mathbf{M} = \mathcal{I}(\mathbf{x}) = \mathbb{E} \left\{ \left(\frac{\partial}{\partial \mathbf{x}} \ln f(\rho | \mathbf{x}) \right) \left(\frac{\partial}{\partial \mathbf{x}} \ln f(\rho | \mathbf{x}) \right)^T \right\}. \quad (51)$$

The partial derivative of $\ln f(\rho | \mathbf{x})$ with respect to \mathbf{x} is

$$\frac{\partial}{\partial \mathbf{x}} \ln f(\rho | \mathbf{x}) = -\frac{\partial \rho^T}{\partial \mathbf{x}} \mathbf{R}^{-1} (\hat{\rho} - \rho) = -\mathbf{H}^T \mathbf{R}^{-1} (\hat{\rho} - \rho) \quad (52)$$

where \mathbf{H} is the Jacobian matrix of $\rho(\mathbf{x})$ in (2) with respect to the true value of \mathbf{x}

$$\mathbf{H} = [\mathbf{G} \ \mathbf{1}_N] \quad (53)$$

with $\mathbf{G} \triangleq [([r - t_1]/\|r - t_1\|), \dots, ([r - t_N]/\|r - t_N\|)]^T$. Inserting (52) into (51) gives the FIM as

$$\begin{aligned} \mathbf{M} &= \mathbb{E}\{\mathbf{H}^T \mathbf{R}^{-1} (\hat{\rho} - \rho) (\hat{\rho} - \rho)^T \mathbf{R}^{-1} \mathbf{H}\} \\ &= \mathbf{H}^T \mathbf{R}^{-1} \mathbb{E}\{(\hat{\rho} - \rho) (\hat{\rho} - \rho)^T\} \mathbf{R}^{-1} \mathbf{H} \\ &= \mathbf{H}^T \mathbf{R}^{-1} \mathbf{H}. \end{aligned} \quad (54)$$

The unknown vector is $\mathbf{x} = [r^T, b]^T$. From the Gaussian density, the CRLB is

$$\text{CRLB}_{\mathbf{r}}([r, b]^T) = \left(\left[\frac{\partial \rho}{\partial r}, \frac{\partial \rho}{\partial b} \right]^T \mathbf{R}^{-1} \left[\frac{\partial \rho}{\partial r}, \frac{\partial \rho}{\partial b} \right] \right)^{-1}. \quad (55)$$

From the model (2), we have $\partial \rho / \partial r^T = \nabla_r$ and $\partial \rho / \partial b = \mathbf{1}_N$. Hence

$$\begin{aligned} \text{CRLB}_{\mathbf{r}}([r_t, b]^T) &= \left(\begin{array}{c} \mathbf{X} \ \mathbf{m} \\ \mathbf{m}^T \ z \end{array} \right)^{-1} \end{aligned} \quad (56)$$

where

$$\mathbf{X} = \nabla_r^T \mathbf{R}^{-1} \nabla_r \quad (57)$$

$$\mathbf{m} = \nabla_r^T \mathbf{R}^{-1} \mathbf{1}_N \quad (58)$$

$$z = \mathbf{1}_N^T \mathbf{R}^{-1} \mathbf{1}_N. \quad (59)$$

B. Optimal UE Placement

This section establishes the lower bound for the determinant of the target estimation error covariance, also known as the D-optimality criterion. The derivation of the CRLB in TOA-based UE localization is of paramount significance as it provides a theoretical benchmark for evaluating localization performance, guides the design of robust localization algorithms, and contributes to improving localization accuracy in scenarios with independent measurement noise and varying variances. This analysis assumes independent measurement noise and delineates an optimal gNB arrangement that attains this bound. The selection of the D-optimality criterion is rooted in its equivalence to minimizing the volume of the errors ellipsoid [28]. The outcomes of this analysis are encapsulated in the subsequent two theorems. Crucially, these theorem findings are relevant to both cellular and radar systems, and they encompass a broader context involving gNB arrays conducting pseudorange measurements on a UE.

Theorem 3: Let $N \geq 3$ be an arbitrary number of available gNBs. Then, under the premise that the obtained pseudorange measurements are modeled according to (2), the determinant of the target estimation error covariance \mathbf{P} is lower bounded by

$$\det[\mathbf{P}] = \frac{1}{\det[\mathbf{M}]} \geq \frac{4\sigma^6}{N^3}. \quad (60)$$

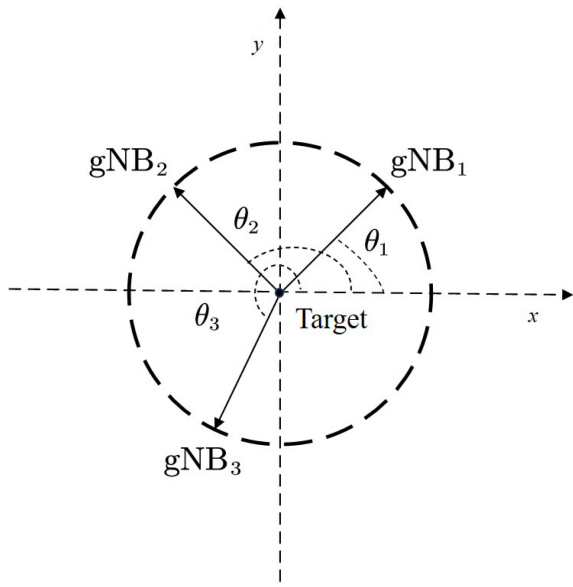


Fig. 2. TOA-based localization, where the unit LOS vectors are reparameterized by the bearing angles between a set of gNBs and a target.

Proof: First, given the CRLB in (56), the matrix \mathbf{H} is reparameterized by the bearing angles $\{\theta_i\}_{i=1}^N$ between the UE and the N gNBs, where θ_i represents the angle between the x -axis and the range vector connecting the UE and the i th gNB, as illustrated in Fig. 2. The matrix \mathbf{M} is given by

$$\mathbf{M} = \mathbf{P}^{-1} = \mathbf{H}^T \mathbf{R}^{-1} \mathbf{H} = \begin{bmatrix} \mathbf{G}^T \mathbf{R}^{-1} \mathbf{G} & \mathbf{G}^T \mathbf{R}^{-1} \mathbf{1}_N \\ \mathbf{1}_N^T \mathbf{R}^{-1} \mathbf{G} & \mathbf{1}_N^T \mathbf{R}^{-1} \mathbf{1}_N \end{bmatrix} \quad (61)$$

where an alternative expression for \mathbf{G} is given by

$$\mathbf{G} = \begin{bmatrix} \mathbf{p} \\ \mathbf{q} \end{bmatrix}^T = \begin{bmatrix} \cos \theta_1 & \cos \theta_2 & \dots & \cos \theta_N \\ \sin \theta_1 & \cos \theta_2 & \dots & \sin \theta_N \end{bmatrix}^T. \quad (62)$$

Fig. 2 depicts the concept of UE localization, where the unit LOS vectors are reparameterized using bearing angles between a group of gNBs and a UE. To facilitate the analysis, let us redefine FIM as a partitioned matrix form given by

$$\mathbf{M} \triangleq \begin{bmatrix} \mathbf{X} & \mathbf{m} \\ \mathbf{m}^T & z \end{bmatrix}. \quad (63)$$

Then, we have the following lemma.

Lemma 3: If the matrix \mathbf{G} is full column-rank, which is assured when a minimum of three gNBs are noncollinear, we obtain the following:

$$0 \prec \mathbf{X} - \frac{1}{z} \mathbf{m} \mathbf{m}^T \leq \mathbf{X}. \quad (64)$$

Proof: See Appendix A. ■

By using the Schur complement properties, Lemma 3 shows the matrix measure (determinant) of $\mathbf{X} - (1/z)\mathbf{m}\mathbf{m}^T$ is smaller than that of \mathbf{X} . Note that

$$\det [\mathbf{M}] \leq \sum_{i=1}^N \sigma_i^{-2} \sum_{1 \leq i < j \leq N} \sigma_i^{-2} \sigma_j^{-2} \sin^2(\theta_j - \theta_i). \quad (65)$$

The derivation of (65) is presented in detail in Appendix B. The structure of $\det[\mathbf{M}]$ reveals that the determinant is

influenced by both the measurement accuracy (σ_i^2, σ_j^2) and the angle θ between the x -axis and the range vector connecting the UE and the i th gNB. These two contributions can be separated only if all the independent measurement errors share the same standard deviation. Specifically, $\sigma_i^2 = \sigma_j^2 \triangleq \sigma^2$ is necessary for expressing $\det[\mathbf{M}]$ as the product of σ^2 and the angle θ , as shown in

$$\begin{aligned} \det [\mathbf{M}] &\leq \sum_{i=1}^N \sigma^{-2} \sum_{1 \leq i < j \leq N} \sigma^{-2} \sigma^{-2} \sin^2(\theta_j - \theta_i) \\ &= N \sigma^{-6} \sum_{1 \leq i < j \leq N} \sin^2(\theta_j - \theta_i) \end{aligned} \quad (66)$$

which agrees with the result obtained in [29] and [30]. The maximum determinant of the \mathbf{M} is attained when $\theta_i = 2\pi \cdot i/N$ [29]. Partial term of (66) can be derived as

$$\begin{aligned} \sum_{1 \leq i < j \leq N} \sin^2(\theta_j - \theta_i) &= \sum_{1 \leq i < j \leq N} \sin^2 \frac{(j-i)2\pi}{N} \\ &= \frac{1}{2} \sum_{i=1}^N \sum_{j=1}^N \sin^2 \frac{(j-i)2\pi}{N} = \frac{1}{2} \sum_{i=1}^N \frac{N}{2} = \frac{N^2}{4}. \end{aligned} \quad (67)$$

The determinant of the \mathbf{M} is further deduced as

$$\det [\mathbf{M}] = \frac{N^3}{4\sigma^6}. \quad (68)$$

Let $N \geq 3$ be an arbitrary number of available gNBs. Then, under the assumption that the obtained pseudorange measurements (with all measurement errors having the same standard deviation) are modeled according to (2), the determinant of the target estimation error covariance matrix \mathbf{P} is ensured to have a lower bound as follows:

$$\det [\mathbf{P}] = \frac{1}{\det [\mathbf{M}]} \geq \frac{4\sigma^6}{N^3}. \quad (69)$$

Up to this point, we have established a lower bound for the target estimation error covariance. The overall system performance is heavily influenced by two key parameters: 1) the measurement noise variance σ_i^2 , as mentioned in [31] and 2) the number of gNBs, denoted as N . These parameters are pivotal in determining the system's effectiveness. In applications, such as target tracking or cellular localization, the target state components, which usually include position, velocity, UE's clock bias, and sometimes gNB's clock bias, may have different orders of magnitude.

In some cases, it may be beneficial to separate the position and velocity terms and other components within the covariance matrix before converting it into a scalar measure, as discussed in [32]. In the context of UE localization, our primary focus is on positioning accuracy, which is essentially the determinant of the resulting target position estimation error covariance, denoted as $\log \det [\mathbf{P}_r]$. In the following sections, we will first derive the specific expression of the estimation error covariance in Theorem 4, and then present the determinant of the resulting target position estimation error covariance in Corollary 4.

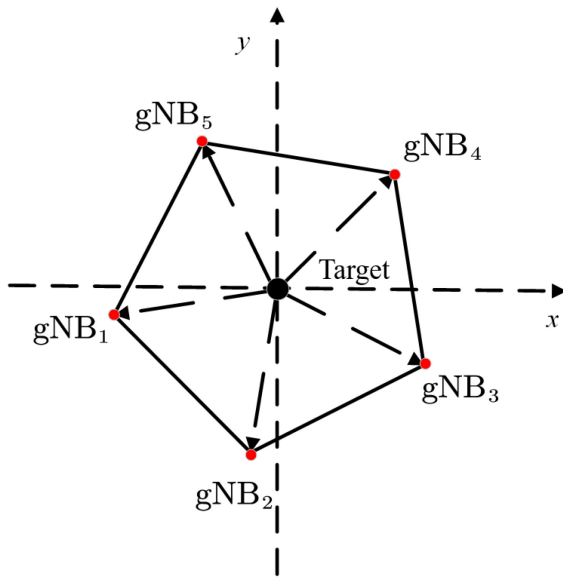


Fig. 3. Optimal gNB-target geometry configuration (e.g., five-sided regular polygon).

The preceding Theorem 3 has established that the estimation error covariance lower bound, as provided in Theorem 3, serves as a lower bound for two parameters related to the measurement noise variance. In the subsequent Theorem 4, we will demonstrate that the specific expression of the estimation error covariance is attainable through an optimal gNB-UE geometry configuration.

Theorem 4: Given a set of N gNBs grouped into L sets, where each set contains $N_l \geq 3$ gNBs with TOA measurements sharing the same noise covariance and each set of gNBs forms a regular polygon around the UE as depicted in Fig. 3, specifically

$$\theta_{i_l}^{(l)} = 2\pi \cdot i_l/N_l + \theta_0^{(l)}, i_l = 1, \dots, N_l \quad (70)$$

where $\theta_{i_l}^{(l)}$ is the bearing angle between the UE and the i_l th gNB in the l th set, and $\theta_0^{(l)}$ is an arbitrary offset angle, the covariance of the UE state estimate is given by

$$\mathbf{P} = \begin{bmatrix} \frac{2}{\sum_{l=1}^L N_l \sigma_l^{-2}} & 0 & 0 \\ 0 & \frac{2}{\sum_{l=1}^L N_l \sigma_l^{-2}} & 0 \\ 0 & 0 & \frac{1}{\sum_{i=l}^L N_i \sigma_i^{-2}} \end{bmatrix}. \quad (71)$$

Proof: We begin this proof by rewriting the information matrix as

$$\mathbf{M} = \begin{bmatrix} \mathbf{p}^T \mathbf{R}^{-1} \mathbf{p} & \mathbf{p}^T \mathbf{R}^{-1} \mathbf{q} & \mathbf{p}^T \mathbf{R}^{-1} \mathbf{1}_N \\ \mathbf{q}^T \mathbf{R}^{-1} \mathbf{p} & \mathbf{q}^T \mathbf{R}^{-1} \mathbf{q} & \mathbf{q}^T \mathbf{R}^{-1} \mathbf{1}_N \\ \mathbf{1}_N^T \mathbf{R}^{-1} \mathbf{p} & \mathbf{1}_N^T \mathbf{R}^{-1} \mathbf{q} & \mathbf{1}_N^T \mathbf{R}^{-1} \mathbf{1}_N \end{bmatrix} \quad (72)$$

where the partitioned vectors are given by

$$\mathbf{p} \triangleq [\mathbf{p}_1 \cdots \mathbf{p}_L]^T, \mathbf{q} \triangleq [\mathbf{q}_1 \cdots \mathbf{q}_L]^T \quad (73)$$

with $\mathbf{p}_l = [\cos \theta_1^{(l)}, \dots, \cos \theta_{N_l}^{(l)}]$ and $\mathbf{q}_l = [\sin \theta_1^{(l)}, \dots, \sin \theta_{N_l}^{(l)}]$, where $l = 1, \dots, L$. Then, the measurement noise covariance is derived as

$$\mathbf{R}^{-1} \triangleq \text{diag}[\Sigma_1^{-1}, \dots, \Sigma_L^{-1}] \quad (74)$$

where $\Sigma_l^{-1} = \text{diag}[\sigma_l^{-2}, \dots, \sigma_l^{-2}]$. Therefore, we conclude that

$$\begin{aligned} \mathbf{p}^T \mathbf{R}^{-1} \mathbf{p} &= \sum_{l=1}^L \mathbf{p}_l^T \sigma_l^{-2} \mathbf{p}_l \\ &= \sum_{l=1}^L \sum_{i_l=1}^{N_l} \sigma_l^{-2} \cos^2 \theta_{i_l}^{(l)} = \sum_{l=1}^L \sigma_l^{-2} \sum_{i_l=1}^{N_l} \cos^2 \theta_{i_l}^{(l)} \end{aligned} \quad (75)$$

$$\mathbf{q}^T \mathbf{R}^{-1} \mathbf{q} = \sum_{l=1}^L \sigma_l^{-2} \sum_{i_l=1}^{N_l} \sin^2 \theta_{i_l}^{(l)} \quad (76)$$

$$\mathbf{1}_N^T \mathbf{R}^{-1} \mathbf{1}_N = \sum_{l=1}^L \sigma_l^{-2} N_l \quad (77)$$

$$\mathbf{p}^T \mathbf{R}^{-1} \mathbf{1}_N = \sum_{l=1}^L \sigma_l^{-2} \sum_{i_l=1}^{N_l} \cos \theta_{i_l}^{(l)} \quad (78)$$

$$\mathbf{q}^T \mathbf{R}^{-1} \mathbf{1}_N = \sum_{l=1}^L \sigma_l^{-2} \sum_{i_l=1}^{N_l} \sin \theta_{i_l}^{(l)} \quad (79)$$

$$\mathbf{p}^T \mathbf{R}^{-1} \mathbf{q} = \sum_{l=1}^L \sigma_l^{-2} \sum_{i_l=1}^{N_l} \sin \theta_{i_l}^{(l)} \cos \theta_{i_l}^{(l)}. \quad (80)$$

Using the Fourier summation formulas [33], we obtain

$$\sum_{i_l=1}^{N_l} \sin^2 \theta_{i_l} = \sum_{i_l=1}^{N_l} \cos^2 \theta_{i_l} = N_l/2 \quad (81)$$

$$\sum_{i_l=1}^{N_l} \sin \theta_{i_l} \cos \theta_{i_l} = \sum_{i_l=1}^{N_l} \cos \theta_{i_l} = \sum_{i_l=1}^{N_l} \sin \theta_{i_l} = 0. \quad (82)$$

Hence, we obtain

$$\mathbf{P} = \begin{bmatrix} \frac{2}{\sum_{l=1}^L N_l \sigma_l^{-2}} & 0 & 0 \\ 0 & \frac{2}{\sum_{l=1}^L N_l \sigma_l^{-2}} & 0 \\ 0 & 0 & \frac{1}{\sum_{l=1}^L N_l \sigma_l^{-2}} \end{bmatrix} \quad (83)$$

which completes the proof. ■

Corollary 3: Since $\text{trace}(\mathbf{R}^{-1}) = \sum_{i=1}^N \sigma_i^{-2} = \sum_{l=1}^{N_l} N_l \sigma_l^{-2}$, the determinant lower bound of estimation error covariance becomes $\det[\mathbf{P}] \geq (4/\text{trace}(\mathbf{R}^{-1}))^3$. Only if $\sigma_i^2 = \sigma^2$ can the lower bound be simplified to

$$\det[\mathbf{P}] \geq \frac{4\sigma^6}{N^3}. \quad (84)$$

Proof: This can be obtained by the product of diagonal elements of estimation error covariance \mathbf{P} [c.f. (83)]. ■

By Corollary 3, the optimal gNB-UE geometry configuration described in Theorem 4 can achieve the determinant lower bound of estimation error covariance established in Theorem 3. In what follows, the determinant of the resulting target position estimation error covariance is derived.

Corollary 4: For the given measurement noise covariance σ_i^2 , the determinant of resulting target position estimation error covariance \mathbf{P}_r is derived as

$$\log \det [\mathbf{P}_r] = \log \left[4 \left(\frac{1}{\sum_{i=1}^N \frac{1}{\sigma_i^2}} \right)^2 \right]. \quad (85)$$

Proof: By applying Theorem 4, the optimal target estimation error covariance can be determined from (83), resulting in the following expression:

$$\mathbf{P} = \begin{bmatrix} \mathbf{P}_r & \mathbf{0}_2 \\ \mathbf{0}_{1 \times 2} & (\sigma_d)^2 \end{bmatrix} = \begin{bmatrix} 2\sigma_r^2 \mathbf{I}_{2 \times 2} & \mathbf{0}_2 \\ \mathbf{0}_{1 \times 2} & \sigma_{eq}^2 \end{bmatrix} \quad (86)$$

$$\text{where } \sigma_r^2 \triangleq \frac{1}{\text{trace}(\mathbf{R}^{-1})} = \frac{1}{(1/\sigma_1^2) + \dots + (1/\sigma_N^2)}.$$

Then, the determinant of each resulting target position estimation error covariance \mathbf{P}_r is given by

$$\log \det [\mathbf{P}_r] = \log \left[4 \left(\frac{1}{\sum_{i=1}^N \frac{1}{\sigma_i^2}} \right)^2 \right] \quad (87)$$

from which we finally obtain (85) and complete this proof. ■

The problem of target localization entails the estimation of a target's position from measurements affected by noise. The results presented in Theorems 3 and 4 find relevance in systems related to UE localization, resembling an optimal sensor placement problem where gNBs are strategically arranged to minimize errors. Consequently, Theorem 4 and Corollary 4 can serve as guidance for system configurations (e.g., regular polygon placement) to achieve the desired performance. Studying the optimal UE placement holds significance. While the analysis may not have direct applicability, it can serve as a valuable tool for system designers. For instance, it can be utilized to assess the system's performance. When the system fails to meet requirements, additional gNBs or the consideration of multisensor fusion becomes imperative to enhance localization accuracy.

The existing literature tackles the issue of optimal gNB placement through the lens of optimal motion control and parameter uncertainty optimization problems, as discussed in [34]. Optimal control focuses on optimizing the gNB trajectories, such as UAVs, to minimize estimation uncertainties. However, it often lacks closed-form solutions, necessitating numerical techniques for resolution. On the other hand, parameter optimization deals with optimal gNB placement analytically, as demonstrated in this section and similar studies [29], [35], [36], [37]. This approach provides insights into how the geometry of the gNB-UE configuration impacts localization, thereby aiding in the optimization of performance, fuel efficiency, and adherence to communication constraints.

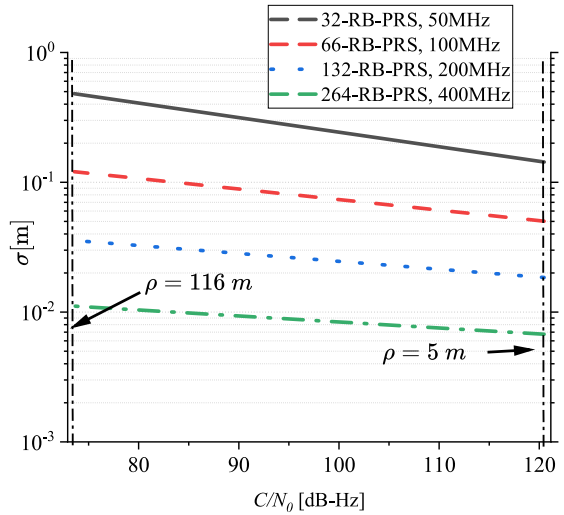


Fig. 4. Plot of σ as a function of the carrier-to-noise ratio C/N_0 by using different 5G system bandwidths, and considering the possible range of C/N_0 in the 5G scenario.

VI. SIMULATION RESULTS

In this section, simulations are employed to substantiate the developed theory, verify the effectiveness of the two proposed localization algorithms, and confirm the optimal gNB placement.

A. Positioning Performance

Fig. 4 depicts the relationship between σ and the carrier-to-noise ratio C/N_0 across various 5G system bandwidths, taking into account the potential range of C/N_0 in the context of a 5G scenario. The C/N_0 limits are defined for two primary network designs characterized by high and low intersite distances (ISDs), denoted as ρ with values of 116 and 5 m, respectively.

The performance analysis of the localization technique presented in this article considers both measurement noise and gNB position error. Notably, TOA measurement noise and gNB position error are uncorrelated. To evaluate performance, we compare the lower bound, RW-MM, R-Means, R-WNLS, and RRW-SDR. It is important to highlight that in scenarios without gNB position errors, we utilize the CRLB, as outlined in Section V. However, when gNB position errors are present, we switch to the CRLB-TOA method, as detailed in Xu's work [38]. The simulation is implemented on a Dell laptop with an Intel Core i7 processor and 16GB RAM, utilizing MATLAB software.

Scenario 1 (No gNB Position Errors): In this scenario, we locate four gNBs in a 2-D area at coordinates $t_1 = [120 \ 120]^T$, $t_2 = [-120 \ 120]^T$, $t_3 = [120 \ -120]^T$, and $t_4 = [-120 \ -120]^T$. The performance measure used is the root-mean-square error (RMSE), calculated as follows:

$$\text{RMSE} = \sqrt{\frac{1}{K} \sum_{i=1}^K \|\mathbf{p} - \hat{\mathbf{p}}\|^2} \quad (88)$$

where $\hat{\mathbf{p}}$ is the estimated target position, K represents the Monte Carlo number. We assess the UE position's RMSE

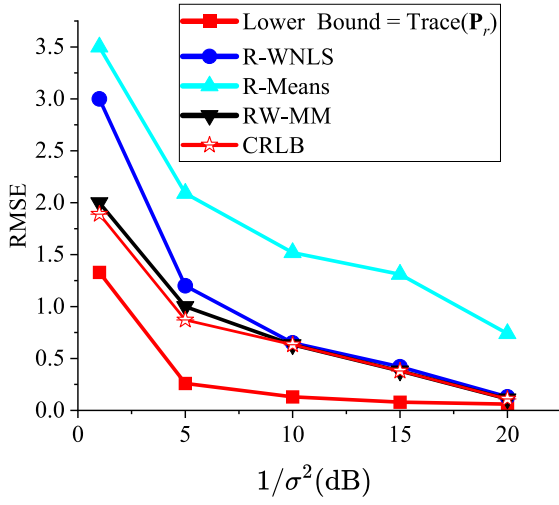


Fig. 5. Comparison of RW-MM, R-WNLS, and R-means algorithms for UE localization without gNB position errors.

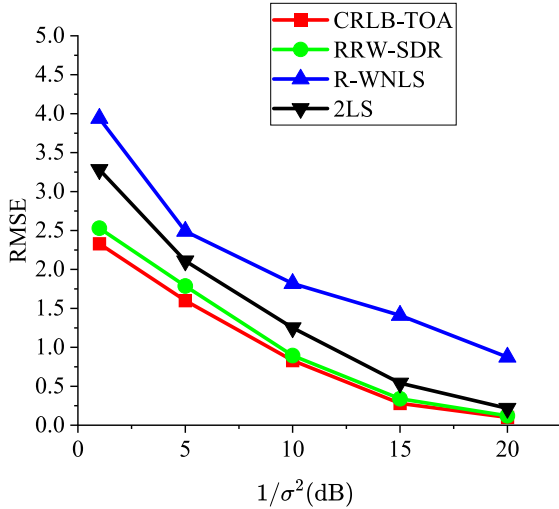


Fig. 6. Comparison of RRW-SDR, R-WNLS, and 2LS algorithms for UE (inside the convex hull) localization with gNB position errors.

as the performance metric across various levels of noise standard deviation. The noise is generated as independent and identically distributed (i.i.d.) Gaussian, with a random selection from a normal distribution of zero mean and a variance of 1. In Fig. 5, we compare the performance of the RW-MM, R-Means, and R-WNLS algorithms. It is evident that the new RW-MM algorithm outperforms R-Means and R-WNLS methods and is close to CRLB. It is seen that the WLNS method is able to achieve the CRLB unless the noise is very large. In contrast, the R-Means method is unable to achieve this, even when the noise is very small.

In the subsequent analysis, we assess the performance of our proposed algorithm for UE localization across varying measurement variances, taking into account gNB position errors. The simulation comprises 1000 Monte Carlo runs with a threshold set at $\delta = 3$. We present simulation results for our RRW-SDR method, R-WNLS, and 2LS, as per Xu et al.'s work [38], alongside the CRLB for TOA in Figs. 5–9, covering scenarios both within and outside the convex hull.

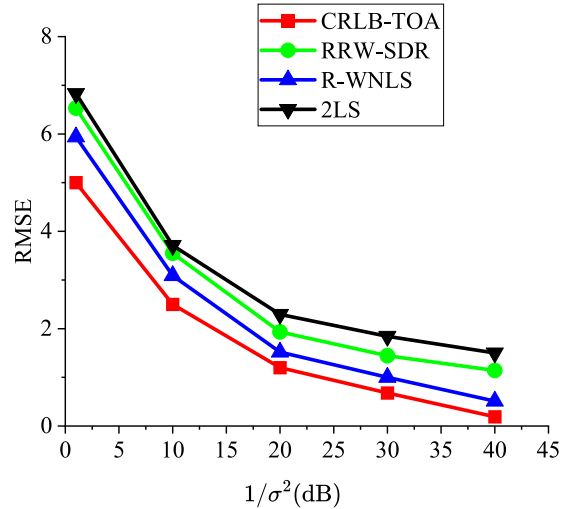


Fig. 7. Comparison of RRW-SDR, R-WNLS, and 2LS algorithms for UE (outside the convex hull) localization with gNB position errors.

Scenario 2 (The UE is Inside the Convex Hull): First, the UE is located at $\mathbf{p} = [1 \ 3]^T$, which falls inside the convex hull created by the gNBs. The performance of the different algorithms in this scenario within the convex hull is depicted in Fig. 6. Notably, the new TOA algorithms show superior performance compared to the R-WNLS and 2LS approaches.

Scenario 3 (The UE is Outside the Convex Hull): The UE is placed at $\mathbf{p} = [200 \ 3]^T$, which is outside the convex hull formed by the four gNBs. The performance of the various algorithms for the scenario outside the convex hull are given in Fig. 7.

Based on the obtained results, it is clear that R-WNLS outperforms the other methods. Unfortunately, both RRW-SDR and 2LS fail to provide accurate estimations in this specific scenario. One contributing factor is the significant distance between the UE and the limitations of SDP optimization to escape local minima. Furthermore, a significant observation is the substantial gap between the CRLB-TOA and the performance of all tested algorithms. This observation underscores the potential for significant improvements in UE localization within the TOA model. Therefore, there is a compelling need to pursue the development of novel and more robust algorithms to enhance the accuracy of UE localization based on TOA measurements.

Scenario 4: In the previous scenarios, we assumed that both the UE position and the N gNBs' positions were fixed. To assess the performance of the RRW-SDR method in a scenario with randomly distributed topology, we randomly position the UE within a square area. For scenarios where the UE is situated inside the convex hull of the gNBs, the area is defined as $\{(c, d) | -120 \leq c \leq 120, -120 \leq d \leq 120\}$. For scenarios where the UE is outside the convex hull, the area is defined as $\{(c, d) | -120 \leq c \leq 120, -300 \leq d \leq 500\}$. Figs. 8 and 9 present the RMSE results for various methods, including the CRLB. It is evident that our proposed RRW-SDR method outperforms 2LS in both scenarios, whether the UE is inside or outside the convex hull. When the UE is within the convex hull, the two robust UE localization methods outperform the

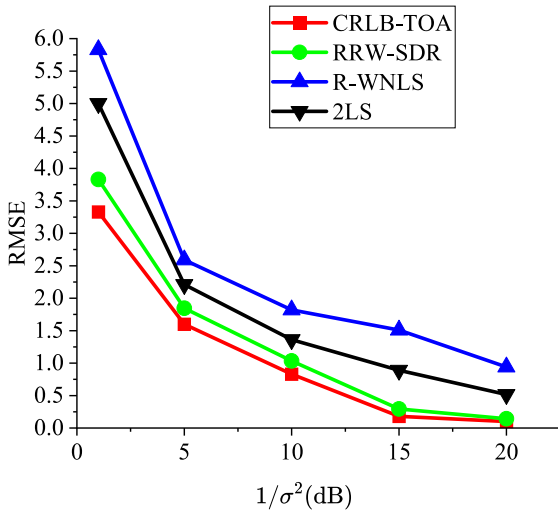


Fig. 8. Comparison of RRW-SDR, R-WNLS, and 2LS algorithms for UE localization inside the convex hull with gNB position errors in a randomly located UE area $\{(c, d) | -120 \leq c \leq 120, -120 \leq d \leq 120\}$.

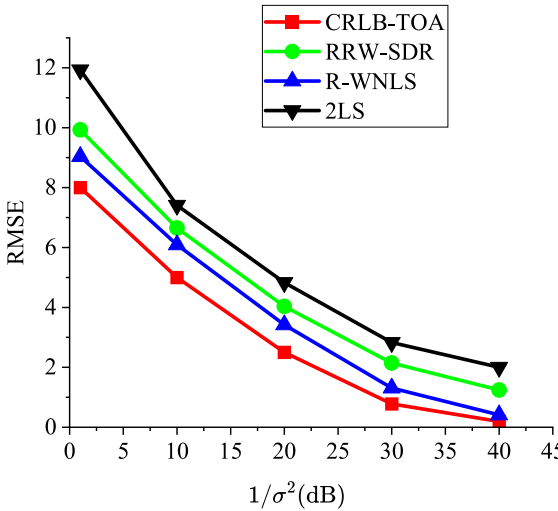


Fig. 9. Comparison of RRW-SDR, R-WNLS, and 2LS algorithms for UE localization outside the convex hull with gNB position errors in a randomly located UE area $\{(c, d) | -120 \leq c \leq 120, -300 \leq d \leq 500\}$.

WNLS method, which does not consider gNB position errors. However, when the UE is outside the convex hull, the WNLS method performs better than the two robust UE localization methods.

The positioning results obtained from the comprehensive numerical evaluations are illustrated in Fig. 10. It can be observed from Fig. 10 that the positioning performance improves as the number of gNBs increases. Fig. 11 indicates that as the bandwidth with an ISD of 25 m increases, the accuracy of both positioning algorithms also improves. Because the RRW-SDR method accounts for BS errors, its accuracy is higher than that of the RW-MM method.

B. Optimal Geometry Analysis

In this section, our objective is to localize a UE with the use of 6 gNBs. The gNBs are required to be positioned outside a circle with a 150 m radius. It is assumed that the noise variance

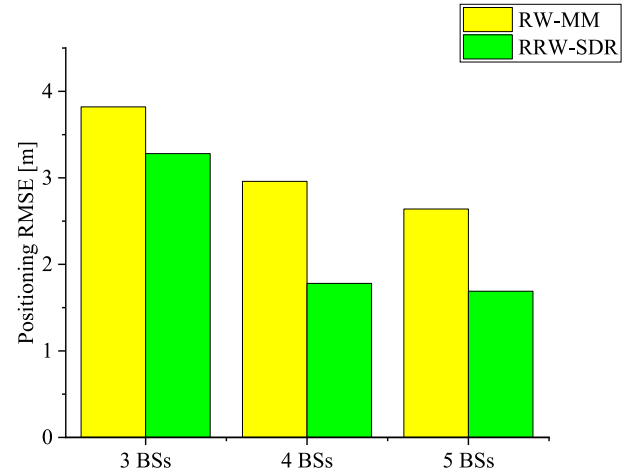


Fig. 10. Comparison of RRW-SDR and RW-MM algorithms for gNB number on the positioning performance.

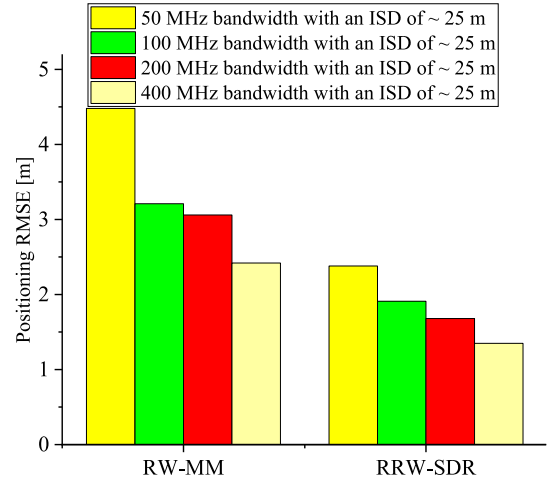


Fig. 11. Effects of the bandwidth on the positioning performance.

for all available gNBs is consistent and given as $\sigma = 1$. In the following, we will investigate the optimal gNB placement in three different scenarios.

Scenario 5: If we consider a UE located at the origin, Theorem 1 suggests that the following gNB placement is optimal:

$$\mathbf{x}_i = \rho_0 \cos \theta_i^*, \mathbf{y}_i = \rho_0 \sin \theta_i^* \quad (89)$$

where $0 \leq \rho_0 \leq 5$ and $\theta_i^* = 2\pi i / 6$. In this case, it is evident that the optimal geometry relies solely on the angular arrangement and is not affected by the distances between gNBs and the UE. One of the optimal configurations for this scenario is illustrated in Fig. 12.

Scenario 6: In this scenario, we are exploring how gNB failures can affect system performance, which could be caused by factors like insufficient power reception, gNB malfunction, disconnection, and others. Let us focus on scenario 6, where one gNB has failed. Despite the gNB failure, the UE localization task is still achievable, albeit with a slight reduction in accuracy. The determinant value in this situation is 28.65, only

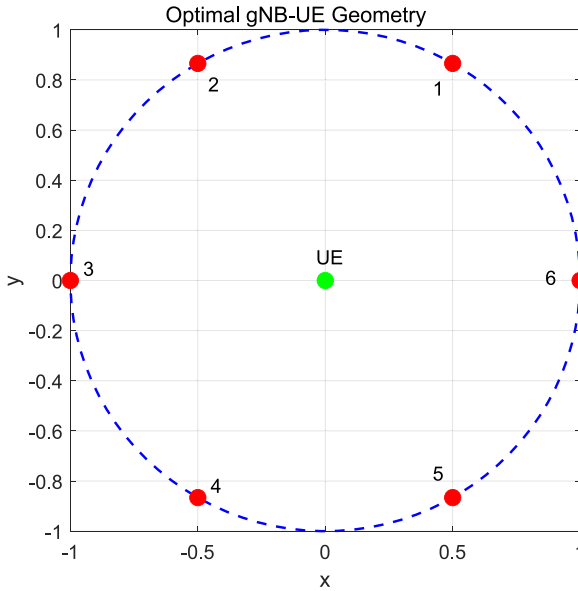


Fig. 12. Optimal gNB-target geometry in scenario 7.

TABLE I
IMPACT OF DAMAGED GNBS ON UE LOCALIZATION PRECISION

No. of the gNBs	1,2	1,3	1,4	1,5	UUA(4)
determinant	12.23	15.65	14.72	14.53	16

slightly below its theoretical maximum of 31.25, calculated as $5^3/4$. This decrease in accuracy is relatively minor.

Scenario 7: Now, let us consider a scenario in which two gNBs have failed. The determinant of the FIM varies depending on how the failed gNBs are arranged. This comparison is elaborated in Table I, with the optimal gNB-target geometry referred to as the uniform angular array (UAA). It is worth noting that when the failed gNBs are positioned close to each other (for example, gNBs 1 and 2), the decline in performance is more noticeable. However, the determinant value remains acceptable even in such cases. Despite the presence of damaged gNBs, the initial configuration of the 6-gNB UAA continues to perform reasonably well.

VII. CONCLUSION

In summary, this study developed new methods and optimal geometry analysis for the challenging problem of UE localization in 5G environments. We introduced the RW-MM algorithm, a practical method based on MM techniques for UE localization. Our analysis established its monotonicity and convergence properties, providing a reasonable theoretical basis. Additionally, we presented RRW-SDR, a novel 5G localization approach tailored for scenarios with bounded gNB position errors. RRW-SDR optimizes the *worst-case* weighted least squares function while addressing individual gNB errors, improving localization accuracy. Furthermore, we derived the CRLB for 5G localization using range measurements, along with a lower bound on the determinant of the target estimation error covariance, particularly relevant for independent

measurement noise with varying variances. We also identified an optimal UE-gNB geometrical configuration to attain this lower bound. Our contributions were validated through extensive numerical simulations, demonstrating the practical robustness and utility of these methods in UE localization scenarios. This article concentrates on 5G applications, such as autonomous driving, distinct from reconfigurable intelligent surfaces (RISs)-aided localization for 6G scenarios [39]. While RIS modifies signal reflections by adjusting phase shifts to enhance localization precision, we do not directly address this aspect. However, the methodology proposed in our paper holds promise for potential application in RIS scenarios in future research. Moreover, future research endeavors could extend the capabilities of 5G positioning systems toward the realm of GNSS/5G navigation, particularly focusing on advancing high-precision positioning solutions tailored for urban environments.

APPENDIX A PROOF OF LEMMA 3

Substitute \mathbf{G} into each block matrix to obtain

$$\mathbf{X} = \mathbf{G}^T \mathbf{R}^{-1} \mathbf{G} = \begin{bmatrix} \sum_{i=1}^N \cos^2 \theta_i \sigma_i^{-2} & \sum_{i=1}^N \cos \theta_i \sin \theta_i \sigma_i^{-2} \\ \sum_{i=1}^N \sin \theta_i \cos \theta_i \sigma_i^{-2} & \sum_{i=1}^N \sin^2 \theta_i \sigma_i^{-2} \end{bmatrix} \quad (90)$$

$$\mathbf{m} = \mathbf{G}^T \mathbf{R}^{-1} \mathbf{1}_N = \begin{bmatrix} \sum_{i=1}^N \cos \theta_i \sigma_i^{-2} \\ \sum_{i=1}^N \sin \theta_i \sigma_i^{-2} \end{bmatrix} \quad (91)$$

$$z = \mathbf{1}_N^T \mathbf{R}^{-1} \mathbf{1}_N = \sum_{i=1}^N \sigma_i^{-2}. \quad (92)$$

Given that $z \in \mathbb{R}$ and utilizing Schur complement properties, the Schur complement of z can be represented as $\mathbf{M}/z = \mathbf{X} - (1/z)\mathbf{mm}^T$.

Under the assumption that \mathbf{G} is full column-rank, which is ensured when a minimum of three gNBs are noncollinear, the matrix \mathbf{X} (i.e., $\mathbf{G}^T \mathbf{R}^{-1} \mathbf{G}$) will be positive-definite.

Therefore, it can be deduced that

$$0 \prec \mathbf{X} - \frac{1}{z} \mathbf{mm}^T \leq \mathbf{X}. \quad (93)$$

APPENDIX B DERIVATION OF (65)

Noting that

$$\begin{aligned} \det[\mathbf{M}] &= z \det \left[\mathbf{X} - \frac{1}{z} \mathbf{mm}^T \right] \\ &\leq z \det[\mathbf{X}] = \sum_{i=1}^N \sigma_i^{-2} \det[\mathbf{X}] \\ &= \sum_{i=1}^N \sigma_i^{-2} \left(\left(\sum_{i=1}^N \cos^2 \theta_i \sigma_i^{-2} \right) \left(\sum_{i=1}^N \sin^2 \theta_i \sigma_i^{-2} \right) \right. \\ &\quad \left. - \left(\sum_{i=1}^N \cos \theta_i \sin \theta_i \sigma_i^{-2} \right)^2 \right) \end{aligned} \quad (94)$$

therefore (94) becomes

$$\begin{aligned} \det [\mathbf{M}] &= \sum_{i=1}^N \sigma_i^{-2} \sum_{i=1}^N \sum_{j=1}^N (\cos^2 \theta_i \sigma_i^{-2} \sin^2 \theta_j \sigma_j^{-2} \\ &\quad - \cos \theta_i \sin \theta_i \sigma_i^{-2} \cos \theta_j \sin \theta_j \sigma_j^{-2}) \\ &= \sum_{i=1}^N \sigma_i^{-2} \sum_{i=1}^N \sum_{j=1}^N \cos \theta_i \sigma_i^{-2} \sin \theta_j \sigma_j^{-2} \sin(\theta_j - \theta_i) \\ &= \sum_{i=1}^N \sigma_i^{-2} \sum_{1 \leq i < j \leq N} \sigma_i^{-2} \sigma_j^{-2} \sin^2(\theta_j - \theta_i). \end{aligned} \quad (95)$$

REFERENCES

- [1] Y. Zhang, R. Wang, and Z. Xing, "A robust evolutionary particle filter technique for integrated navigation in urban environments via GNSS and 5G signals," *IEEE Trans. Ind. Informat.*, vol. 20, no. 4, pp. 6866–6878, Apr. 2024.
- [2] Y. Zhang, R. Wang, and Z. Xing, "Collaborative navigation in urban environments via GNSS and 5G signals," in *Proc. IEEE Int. Conf. Commun.*, 2023, pp. 6275–6280.
- [3] Z. Z. M. Kassas, J. Khalife, K. Shamaei, and J. Morales, "I hear, therefore I know where I am: Compensating for GNSS limitations with cellular signals," *IEEE Signal Process. Mag.*, vol. 34, no. 5, pp. 111–124, Sep. 2017.
- [4] M. Maaref, J. Khalife, and Z. M. Kassas, "Lane-level localization and mapping in GNSS-challenged environments by fusing lidar data and cellular pseudoranges," *IEEE Trans. Intell. Veh.*, vol. 4, no. 1, pp. 73–89, Mar. 2019.
- [5] Y. Zhang, X. Tan, and C. Zhao, "UWB/INS integrated pedestrian positioning for robust indoor environments," *IEEE Sensors J.*, vol. 20, no. 23, pp. 14401–14409, Dec. 2020.
- [6] J. Khalife and Z. M. Kassas, "Precise UAV navigation with cellular carrier phase measurements," in *Proc. IEEE/ION Pos., Locat. Navig. Symp. (PLANS)*, 2018, pp. 978–989.
- [7] K. Shamaei and Z. M. Kassas, "Sub-meter accurate UAV navigation and cycle slip detection with LTE carrier phase measurements," in *Proc. ION GNSS*, 2019, pp. 2469–2479.
- [8] Z. M. Kassas, V. Ghadiok, and T. E. Humphreys, "Adaptive estimation of signals of opportunity," in *Proc. ION GNSS*, 2014, pp. 1679–1689.
- [9] J. J. Morales and Z. M. Kassas, "Optimal collaborative mapping of terrestrial transmitters: Receiver placement and performance characterization," *IEEE Trans. Aerosp. Electron. Syst.*, vol. 54, no. 2, pp. 992–1007, Apr. 2018.
- [10] R. M. Vaghefi and R. M. Buehrer, "Cooperative joint synchronization and localization in wireless sensor networks," *IEEE Trans. Signal Process.*, vol. 63, no. 14, pp. 3615–3627, Jul. 2015.
- [11] H. Chen, G. Wang, and N. Ansari, "Improved robust TOA-based localization via NLOS balancing parameter estimation," *IEEE Trans. Veh. Technol.*, vol. 68, no. 6, pp. 6177–6181, Jun. 2019.
- [12] Z. Abu-Shaban, X. Zhou, and T. D. Abhayapala, "A novel TOA-based mobile localization technique under mixed LOS/NLOS conditions for cellular networks," *IEEE Trans. Veh. Technol.*, vol. 65, no. 11, pp. 8841–8853, Nov. 2016.
- [13] S. Xu, Y. Ou, and W. Zheng, "Optimal sensor-target geometries for 3-D static target localization using received-signal-strength measurements," *IEEE Signal Process. Lett.*, vol. 26, no. 7, pp. 966–970, Jul. 2019.
- [14] L. Yang, N. Wu, B. Li, W. Yuan, and L. Hanzo, "Indoor localization based on factor graphs: A unified framework," *IEEE Internet Things J.*, vol. 10, no. 5, pp. 4353–4366, Mar. 2023.
- [15] Y. Xiong, N. Wu, Y. Shen, and M. Z. Win, "Cooperative localization in massive networks," *IEEE Trans. Inf. Theory*, vol. 68, no. 2, pp. 1237–1258, Feb. 2022.
- [16] Y. Xiong, N. Wu, Y. Shen, and M. Z. Win, "Cooperative network synchronization: Asymptotic analysis," *IEEE Trans. Signal Process.*, vol. 66, no. 3, pp. 757–772, Feb. 2018.
- [17] A. A. Abdallah, K. Shamaei, and Z. M. Kassas, "Assessing real 5G signals for opportunistic navigation," in *Proc. ION GNSS*, 2020, pp. 2548–2559.
- [18] E. Christopher, H. S. Dhillon, and R. M. Buehrer, "A statistical characterization of localization performance in wireless networks," *IEEE Trans. Wireless Commun.*, vol. 17, no. 9, pp. 5841–5856, Sep. 2018.
- [19] S. Aditya, H. S. Dhillon, A. F. Molisch, R. M. Buehrer, and H. M. Behairy, "Characterizing the impact of SNR heterogeneity on time-of-arrival-based localization outage probability," *IEEE Trans. Wireless Commun.*, vol. 18, no. 1, pp. 637–649, Jan. 2019.
- [20] M. Koivisto et al., "Joint device positioning and clock synchronization in 5G ultra-dense networks," *IEEE Trans. Wireless Commun.*, vol. 16, no. 5, pp. 2866–2881, May 2017.
- [21] L. Chen, X. Zhou, F. Chen, L.-L. Yang, and R. Chen, "Carrier phase ranging for indoor positioning with 5G NR signals," *IEEE Internet Things J.*, vol. 9, no. 13, pp. 10908–10919, Jul. 2022.
- [22] S. Fan, W. Ni, H. Tian, Z. Huang, and R. Zeng, "Carrier phase-based synchronization and high-accuracy positioning in 5G new radio cellular networks," *IEEE Trans. Commun.*, vol. 70, no. 1, pp. 564–577, Jan. 2022, doi: [10.1109/TCOMM.2021.3119072](https://doi.org/10.1109/TCOMM.2021.3119072).
- [23] K. Shamaei and Z. M. Kassas, "Receiver design and time of arrival estimation for opportunistic localization with 5G signals," *IEEE Trans. Wireless Commun.*, vol. 20, no. 7, pp. 4716–4731, Jul. 2021.
- [24] J. A. del Peral-Rosado, J. A. López-Salcedo, S. Kim, and G. Seco-Granados, "Feasibility study of 5G-based localization for assisted driving," in *Proc. Int. Conf. Localiz. GNSS (ICL-GNSS)*, 2016, pp. 1–6.
- [25] Y. Sun, P. Babu, and D. P. Palomar, "Majorization-minimization algorithms in signal processing, communications, and machine learning," *IEEE Trans. Signal Process.*, vol. 65, no. 3, pp. 794–816, Feb. 2017.
- [26] M. Razaviyayn, M. Hong, and Z.-Q. Luo, "A unified convergence analysis of block successive minimization methods for nonsmooth optimization," *SIAM J. Optim.*, vol. 23, no. 2, pp. 1126–1153, 2013.
- [27] Z.-Q. Luo, W.-K. Ma, A. M.-C. So, Y. Ye, and S. Zhang, "Semidefinite relaxation of quadratic optimization problems," *IEEE Signal Process. Mag.*, vol. 27, no. 3, pp. 20–34, May 2010.
- [28] D. Ucinski, *Optimal Measurement Methods for Distributed Parameter System Identification*. Boca Raton, FL, USA: CRC Press, 2004.
- [29] A. N. Bishop, B. Fidan, B. D. Anderson, K. Doğançay, and P. N. Pathirana, "Optimality analysis of sensor-target localization geometries," *Automatica*, vol. 46, no. 3, pp. 479–492, 2010.
- [30] M. A. Spirito, "On the accuracy of cellular mobile station location estimation," *IEEE Trans. Veh. Technol.*, vol. 50, no. 3, pp. 674–685, May 2001.
- [31] K. Keykhosravi, M. F. Keskin, S. Dwivedi, G. Seco-Granados, and H. Wymeersch, "Semi-passive 3D positioning of multiple RIS-enabled users," *IEEE Trans. Veh. Technol.*, vol. 70, no. 10, pp. 11073–11077, Oct. 2021.
- [32] C. Yang, L. Kaplan, and E. Blasch, "Performance measures of covariance and information matrices in resource management for target state estimation," *IEEE Trans. Aerosp. Electron. Syst.*, vol. 48, no. 3, pp. 2594–2613, Jul. 2012.
- [33] N. Levanon, "Lowest GDOP in 2-D scenarios," *IEE Proc.-Radar, Sonar Navig.*, vol. 147, no. 3, pp. 149–155, 2000.
- [34] S. Zhao, B. M. Chen, and T. H. Lee, "Optimal sensor placement for target localisation and tracking in 2D and 3D," *Int. J. Control.*, vol. 86, no. 10, pp. 1687–1704, 2013.
- [35] L. Rui and K. Ho, "Elliptic localization: Performance study and optimum receiver placement," *IEEE Trans. Signal Process.*, vol. 62, no. 18, pp. 4673–4688, Sep. 2014.
- [36] I. Shames, A. N. Bishop, M. Smith, and B. D. Anderson, "Doppler shift target localization," *IEEE Trans. Aerosp. Electron. Syst.*, vol. 49, no. 1, pp. 266–276, Jan. 2013.
- [37] N. H. Nguyen and K. Doğançay, "Optimal geometry analysis for multistatic TOA localization," *IEEE Trans. Signal Process.*, vol. 64, no. 16, pp. 4180–4193, Aug. 2016.
- [38] E. Xu, Z. Ding, and S. Dasgupta, "Source localization in wireless sensor networks from signal time-of-arrival measurements," *IEEE Trans. Signal Process.*, vol. 59, no. 6, pp. 2887–2897, Jun. 2011.
- [39] Z. Peng, Z. Zhang, C. Pan, M. Di Renzo, O. A. Dobre, and J. Wang, "Beamforming optimization for active RIS-aided multiuser communications with hardware impairments," *IEEE Trans. Wireless Commun.*, early access, Feb. 27, 2024, doi: [10.1109/TWC.2024.3367131](https://doi.org/10.1109/TWC.2024.3367131).